Investigating Transport of Charged Nanoparticles by Multiphoton Fluorescence Correlation Spectroscopy (MPFCS)

by

Ming-Zher Poh

B.S. Electrical and Computer Engineering

Cornell University, 2005

Submitted to the Department of Electrical Engineering and Computer Science

in Partial Fulfillment of the Requirements for the Degree of

Master of Science in Electrical Engineering and Computer Science

at the Massachusetts Institute of Technology

August 2007

[September 2007]

Author_____
Department of Electrical Engineering and Computer Science
August 8, 2007

Certified by_____
Rakesh K. Jain
A. Werk Cook Professor of Radiation Oncology, HMS, MGH
Thesis Supervisor

Accepted by_____
Arthur C. Smith
Professor of Electrical Engineering
Chairman, Department Committee on Graduate Theses

Investigating Transport of Charged Nanoparticles by Multiphoton Fluorescence Correlation Spectroscopy (MPFCS)

by

Ming-Zher Poh

Submitted to the
Department of Electrical Engineering and Computer Science
August 8, 2007

In Partial Fulfillment of the Requirements for the Degree of
Master of Science in Electrical Engineering and Computer Science

ABSTRACT

Nanoparticles have been demonstrated as a promising new generation of specific imaging agents and targeted delivery vehicles for the diagnosis and treatment of solid tumors. Nonetheless, for optimal therapy of tumors, the nanoparticles must penetrate the tumor interstitial matrix to reach the cancer cells. This thesis describes the development of a multiphoton fluorescence correlation spectroscopy (MPFCS) system and its utilization to probe the effect of charge on the diffusion of quantum dot (QD) nanocrystals in collagen and collagen-hyaluronan (HA) composite gel models of human colon adenocarcinoma (LS174T). The MPFCS system was integrated with a multiphoton laser-scanning microscope (MPLSM) to enable visualization of QD distribution and collagen organization, as well as diffusion measurements. QDs of three different charges by modifying the surface of pre-made CdSe/CdZnS QDs with dihydrolipoic acid (DHLA), DHLA-polyethyleneglycol (DHLA-PEG) and amino-functionalized DHLA-PEG (DHLA-PEG-NH_2). Aggregation was observed in QD-DHLA (ξ-potential = -31.12 mV) and QD-DHLA-PEG-NH_2 (ξ-potential = +37.39 mV) samples in gels, but the distribution of QD-DHLA-PEG (ξ-potential = -18.16 mV) was uniform. FCS measurements were performed for each QD sample in both gel models. Experimental data indicated anomalous subdiffusion of QDs in both gels with all samples having the same time exponent. The transport coefficient of QD-DHLA-PEG was significantly higher than QD-DHLA and QD-DHLA-PEG-NH_2. A two-component free diffusion model also provided a good fit for the data, but did not provide a clear picture on the role of charge in diffusion. Our experiments suggest that anionic and cationic nanoparticles experience more hindrance compared to neutral, PEGylated nanoparticles in both collagen and collagen-HA gels.

Thesis Supervisor: Rakesh K. Jain
Title: A. Werk Cook Professor of Radiation Oncology, HMS, MGH

For my Mom and Dad

TABLE OF CONTENTS

List of Figures
List of Tables
List of Abbreviations

CHAPTER 1: INTRODUCTION 10

1.1 Background and Motivation 10

1.2 Objectives 11

1.3 Cancer Nanotechnology 12
1.3.1 Nanotechnology 12
1.3.2 Targeting strategies 14
1.3.3 Quantum Dots 17

1.4 Tumor Interstitium 19
1.4.1 Barriers to Drug Delivery 19
1.4.2 Composition of Tumor Interstitium 21
1.4.2.1 Collagen and Elastin 22
1.4.2.2 Glycosaminoglycans 23
1.4.3 Electrical Charge 24
1.4.4 Interstitial volume exclusion 24
1.4.5 Interstitial Transport 25
1.4.5.1 Dependence on size, configuration charge and binding 26
1.4.5.2 Role of collagen and GAG 27

1.5 Conclusion 28

CHAPTER 2: FLUORESCENCE CORRELATION SPECTROSCOPY 30

2.1 Introduction 30

2.2 Theory of FCS 32

2.3 Multiphoton FCS (MPFCS) 36

CHAPTER 3: INSTRUMENTATION DEVELOPMENT FOR MULTIPHOTON FLUORESCENCE CORRELATION SPECTROSCOPY 39

3.1 Introduction 39

3.2 Experimental realization of MPFCS 40
3.2.1 Optical and hardware setup 40
3.2.2 Software for data analysis 42

3.3 Calibration of MPFCS system 43
3.3.1 Testing the digital correlator card 43
3.3.2 Measurement of laser power at sample 45
3.3.3 Testing the stability of MPFCS setup 45
3.3.4 Characterization of the excitation volume 47
3.3.5 FCS measurements in solution 52
3.3.6 Characterization of the field of view 54

CHAPTER 4: FLUORESCENCE CORRELATION SPECTROSCOPY OF QUANTUM DOTS 56

4.1 Motivation 56

4.2 Characterization of QDs 57

4.3 MPFCS of QDs in solution 58
4.3.1 Results and discussion 59
4.3.1.1 Distribution of QDs in solution 59
4.3.1.2 Curve shape variations 60
4.1.1.1 Diffusion in solution 62

4.4 MPFCS of QDs in gels 63
4.4.1 Methods 63
4.4.2 Results and discussion 64
4.4.2.1 Organization of gels 64
4.4.2.2 Distribution of QDs in gels 66
4.4.2.3 Transport of QDs in gels 70

4.5 Conclusions 80

References

List of Figures

Figure 1. Size of nanoparticles compared to biological entities and other familiar items (Source: McNeil[10]) 14
Figure 2. Schematic of a QD showing an optically active core, a protective inorganic shell an organic cap and one of the organic cap molecules functionalized. 18
Figure 3. Quantum dot spectra. (a) QDs tuned to emit at wavelenghts not shared by signals from GFP and second harmonic generation with 810-nm incident light (green and dark blue lines, respectively). QDs exhibit a narrow and symmetric emission spectra (cyan, yellow and red lines). 18
Figure 4. Optical setup for MPFCS measurements. Laser light (red) is expanded, collimated and focused by a high power objective inside the sample. Fluorescence (green) emitted by excited molecules within the two-photon excitation volume is collected and focused into a PMT with single-photon sensitivity. 41
Figure 5. Testing the digital correlator card. Square waves and sine waves with 5V peak-to-peak voltages were generated at different frequencies and the output of the correlator card recorded. The autocorrelation curves produced show peaks at every time period, *T*, corresponding to the frequency, *f*, of the input signal. 44
Figure 6. Relationship between laser power before X-Y scanbox and laser power at sample. Laser power at the two locations were measured for 4 different settings (red diamonds) and a linear best fit line (blue line) yields the relationship between the two. 45
Figure 7. Test for stability of MPFCS system. Autocorrelation curves of 1 μm (yellow-green) and 0.28 μm (red) fluorescent microspheres stuck on a microscope slide display a flat profile. FCS measurements were performed at 800nm excitation and with 2.9 mW laser power at sample. 47
Figure 8. Effect of correction collar setting on autocorrelation functions. FCS measurements were performed on fluorescent microspheres in solution at 800 nm excitation with constant laser power at the sample (2.9 mW) and different correction collar settings. 48
Figure 9. Relationship between focal volume size and correction collar setting. The focal volume size increases as collar setting increases and its minimum value is around 0.14. 49
Figure 10. Calibration of focal volume size. FCS measurements (blue circles) were performed on a sample of 0.28 μm microspheres in distilled water at 800 nm excitation and 2.9 mW laser power at the sample. A total of five measurements were performed (each 60s long) and averaged before fitting (red line) for r_0 and *K* with *D* fixed at 1.7507×10^{-7} cm^2/s. 50
Figure 11. Diffusion of rhodamine-6G in solution. FCS measurements (green circles) were performed on nM concentration of rhodamine-6G in distilled water at 800 nm excitation and 2.9 mW laser power at the sample. A total of ten measurements (each 120s long) were performed and averaged before fitting (red line) to yield $D = 2.721 \times 10^{-6}$ cm^2/s. 51
Figure 12. FCS performed on a size series of microspheres. Diffusion measurements (red triangles) were performed for microspheres of different sizes (44, 51, 71, 100 nm) in distilled water at 800 nm excitation and 3.6 mW laser power at the sample. Ten measurements (each 15 – 60s) were performed for each different microsphere. Theoretical values (purple diamond) are shown for comparison. 53
Figure 13. Diffusion of albumin in solution. FCS measurements (green circles) were performed on TAMRA-BSA in distilled water at 800 nm excitation and 2.9 mW laser power at the sample. A total of ten measurements (each 120s long) were performed and averaged before fitting (red line) to yield $D = 6.462 \times 10^{-6}$ cm^2/s. 54
Figure 14. Field of view characterization. Images of a stage micrometer taken with an Olympus 20x 0.95 NA (left) and Olympus 60x 1.2 NA (right). Divisions are 10 μm apart. Image sizes are 1024 x 1024 pixels. 55
Figure 15. Chemical structures of molecules used to modify QD surface charges. DHLA was selected to provide a negative charge, DHLA-PEG provides a "neutral" charge and DHLA-PEG-NH_2 provides a positive charge. 57

Figure 16. Images of QD-nanocrystals (Emission max: 650 nm) in phosphate buffer solution (1x PBS) using MPLSM. The distribution of QD nanocrystals (red) modified with DHLA-PEG-NH_2 (A), DHLA-PEG (B), and DHLA (C) are shown in PBS. Images are 223 μm across. 60
Figure 17. Typical FCS curves for QDs recorded at various excitation powers. The amplitude decreases visibly with increasing powers. 60
Figure 18. Excitation rate profile of a fluorescent particle as a function of position and laser excitation power. As laser power is increased, the top of the Gaussian profile is clipped and starts to look like a top-hat, thereby increasing the effective focal volume. 61
Figure 19. FCS curves of QDs with different surface modifications. Experimental data was fitted to a single component free diffusion model (red lines). At least five measurements were taken for....62
Figure 20. Organization of gels. SHG images of collagen gels (left) and collagen-HA composite gels (right) reveal inhomogeneous organization and short, dense fibers. Images are 223 across. 65
Figure 21. Three-dimensional rendering of collagen gel. 86 images were reconstructed, revealing three-dimensional nature of collagen organization. Dimensions are 223 x 223 x 50 μm. 66
Figure 22. Images of QD-nanocrystals in collagen gels using multiphoton microscopy. Distribution of QD nanocrystals (red) modified with DHLA-PEG-NH_2 (A-C), DHLA-PEG (D-F), and DHLA (G-I) are shown in gels composed of collagen type I fibers (green). Images are 630 μm across. 68
Figure 23. Images of QD-nanocrystals in collagen-HA composite gels using multiphoton microscopy. Distribution of QD nanocrystals (red) modified with DHLA-PEG-NH_2 (A-C), DHLA-PEG (D-F), and DHLA (G-I) are shown in gels composed of collagen type I fibers (green). Images are 630 μm across. 69
Figure 24. Typical FCS curve of QD diffusion in gels. A 20s measurement of QD-DHLA-PEG in collagen-HA composite gel was obtained at 800 nm excitation and with 0.7 mW laser power at sample. A single component free diffusion model (equation 12) produced a poor fit for the experimental data. 70
Figure 25. FCS data of QD transport in gels described by anomalous subdiffusion and two-component free diffusion. Anomalous diffusion (purple) and two-component (red) models provided good fits for experimental data. 71
Figure 26. Anomalous diffusion exponent (α) values of QDs in gels. Values were extracted from experimental data fitted to an anomalous diffusion model. There was no significant difference across all samples. α was between 0.4 – 0.47, indicating anomalous subdiffusion. Error bars represent 1 S.E.M. 72
Figure 27. Transport coefficients of QDs in gels. Values were extracted from experimental data fitted to an anomalous diffusion model. * indicates statistical significance between QD-DHLA and QD-DHLA-PEG in collagen-HA ($p < 0.05$). ✠ indicates statistical significance between QD-DHLA-PEG-NH_2 and QD-DHLA-PEG in collagen-HA ($p < 0.05$). ❖ indicates statistical significance between QD-DHLA and QD-DHLA-PEG in collagen ($p < 0.05$). ☆ indicates statistical significance between QD-DHLA-PEG-NH_2 and QD-DHLA-PEG in collagen-HA ($p < 0.05$). Error bars represent 1 S.E.M. 73
Figure 28. Subpopulation fraction of QDs in collagen-HA composite gels. *Experimental data show a significantly higher percentage of QD-DHLA-PEG in the fast component compared to QD-DHLA ($p < 0.05$). Error bars represent 1 S.E.M. 75
Figure 29. Subpopulation fraction of QDs in collagen gels. * Experimental data show a significantly higher percentage of QD-DHLA-PEG in the fast component compared to QD-DHLA ($p < 0.05$). Error bars represent 1 S.E.M. 76
Figure 30. Fast component diffusion coefficients (D_1) of QDs in gels. ✠ Experimental data show a significantly higher diffusion coefficient of QD-DHLA-PEG in the fast component compared to QD-DHLA ($p < 0.05$) in collagen. Error bars represent 1 S.E.M. 77
Figure 31. Slow component diffusion coefficients (D_2) of QDs in gels. ✶ Experimental data show a significantly higher diffusion coefficient of QD-DHLA-PEG than t compared to QD-DHLA in collagen. ✠ Diffusion coefficient of QD-DHLA-PEG-NH2 significantly higher than QD-DHLA

in collagen-HA. ❖ Diffusion coefficient of QD-DHLA significantly higher in collagen-HA vs. collagen. ✧ Diffusion coefficient of QD-DHLA-PEG-NH_2 significantly higher in collagen-HA vs. collagen. For all cases listed, $p < 0.05$. Error bars represent 1 S.E.M. 77

List of Tables

Table 1. Collagen and hyaluronan (HA) content in the interstitial matrix (IM) of human and murine tumors 21
Table 2. Physicochemical properties of QD samples 58
Table 3. Diffusion coefficients and size of QD samples. The error is the standard deviation derived from different measurements. 63

List of Abbreviations

BSA	Bovine serum albumin
ECM	Extracellular matrix
FCS	Fluorescence correlation spectroscopy
FDA	Food and drug administration
FOV	Field of view
FRAP	Fluorescence recovery after photobleaching
FWHM	Full width at half maximum
GAG	Glycosaminoglycan
HA	Hyaluronan
IM	Interstitial matrix
MPE	Multiphoton excitation
MPFCS	Multiphoton fluorescence correlation spectroscopy
MPLSM	Multiphoton laser scanning microscopy
NA	Numerical aperture
PMT	Photomultiplier tube
PSF	Point spread function
QD	Quantum dot
SHG	Second harmonic generation
TPE	Two-photon excitation

Chapter 1: Introduction

1.1 Background and Motivation

Cancer is the leading cause of death among Americans today. Currently, one in four deaths in the United States is due to cancer[1]. Despite outstanding progress in fundamental cancer biology over the past quarter century, these advances have not translated into commensurate advances in the clinic. The main reason for this disparity is the lack of effective administration of therapeutic agents so that they will selectively reach the desired targets with minimum or no collateral damage[2]. Conventional cancer treatments and diagnostics involve chemotherapy, surgery, radiation, biopsy and the application of catheters. Success of cancer therapy is limited due to the lack of early disease detection, nonspecific systemic distribution, inadequate drug concentrations reaching the tumor and the inability to monitor therapeutic responses[1].

Nanotechnology is an emerging field that will potentially result in significant advances in early detection, molecular imaging, assessment of therapeutic efficacy, targeted and multifunctional therapeutics as well as the prevention and control of cancer[2]. The unique size of nanoparticles (1 - 100nm) offers more

surface area and functional groups that can be linked to multiple optical, radioisotopic, or magnetic diagnostic and therapeutic moieties[3]. For example, Abraxane represents a new class of nanoparticles making their way into the clinic and has successfully been used in women with breast cancer initially refractory to texane therapy[4]. Thus, applying to nanotechnology to medicine, in particular to the war against caner, may introduce a new paradigm in healthcare.

While the future of cancer nanotechnology promises looks bright, nanosized hybrid therapeutics and drug delivery systems will not be advantageous unless they (or the drug they release) reach the desired target in effective concentrations[5,6]. Furthermore, poor drug delivery and residence at the target site can result in significant complications, such as multi-drug resistance[7]. In order to use these nanoparticles effectively, there is a need to establish design guidelines for their physicochemical properties that will ensure optimal delivery to tumors.

1.2 Objectives

This thesis describes the development of a multiphoton fluorescence correlation spectroscopy (MPFCS) system and its utilization to probe the effect of charge on the diffusion of nanoparticles in the tumor interstitium. The first objective is to

build a MPFCS system to enable tranport measurements as well as develop software for the analysis of experimental data. Second, we will characterize and calibrate our MPFCS system using fluorescent dyes and microspheres of known diffusion coefficients. Lastly, we will adapt MPFCS to measure the diffusion of charged QDs in solution as well as in gels developed to resemble the tumor interstium. When completed, this information will provide guidelines on the design of nano-vectors for applications such as the delivery of drugs to solid tumors. We begin with a review of the application of nanotechnology in cancer, summarized from various different sources.

1.3 Cancer Nanotechnology

1.3.1 Nanotechnology

Nanotechnology refers to the creation and utilization of materials, devices, and system through the control of matter on the nanometer-length scale. Formal definitions require that the functional structures created have at least one characteristic dimension measured in the 1 - 100nm range. Nonetheless, in Whitesides' definition of nanotechnology[8], he describes the 'right' size in nanobiotechnology in an operational sense, with respect to addressable unmet needs in biology, rather than placing stringent limitations on the exact

dimensions. Others, including Langer and colleagues have also taken a similar standpoint, the former in the context of drug-delivery applications[9].

In the context of biological systems, nanotechnology offers the ability to control the size of the resulting particles and devices. Figure 1 provides a comparison of the size of certain popular nanoparticles, including liposomes, dendrimers, gold nanoshells, quantum dots and fullerenes to familiar items. The diameter of human cells span 10 - 20 μm while the size of cell organelles ranges from a few nanometers to a few hundred nanometers. Typically, nanoscale constructs and devices are smaller than human and around the same size as large biological macromolecules such as enzymes and receptors[10]. These nanoparticles provide a less invasive method of interacting with biomolecules both on the cell surface and within the cells, without altering the behavior and biochemical properties of those molecules[3].

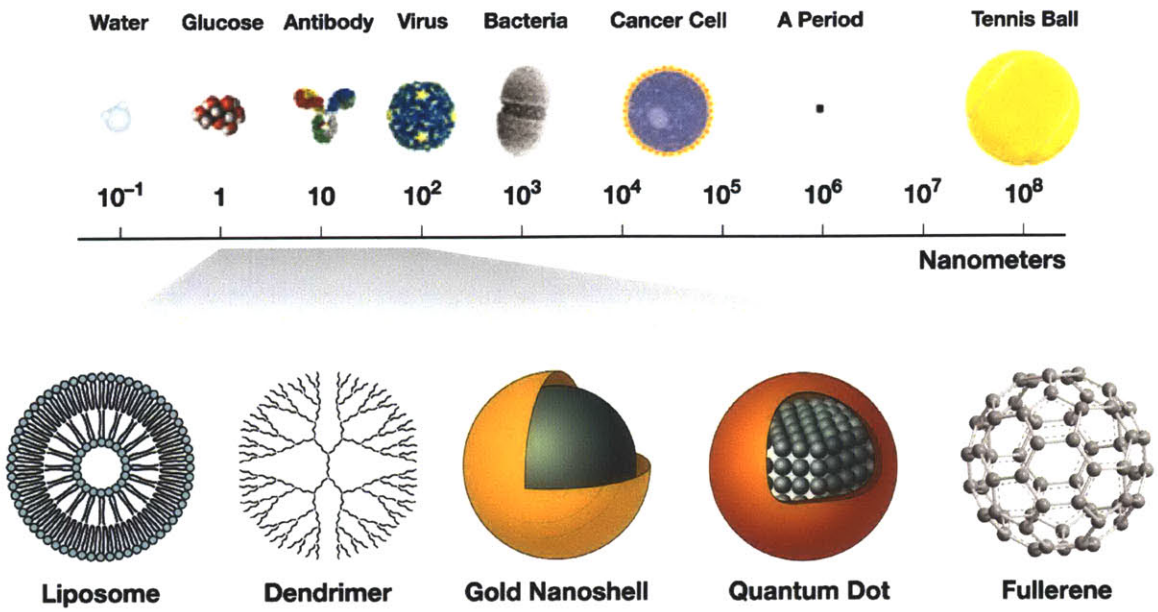

Figure 1. Size of nanoparticles compared to biological entities and other familiar items (Source: McNeil[10])

For drug delivery applications, nanoparticles must be small enough to avoid rapid filtration by the spleen, with filaments spaced roughly 200 nm[11], that form a meshwork for phagocytic cells[12]. Furthermore, the nanoparticles need to be small enough to pass through the liver's fenestrate (150 - 200 nm) and avoid the Kupffer cell-lined sieve plates[13]. Despite their small size, the capacity, or payload of nanoparticles is on the order of tens of thousands of atoms or small molecules.

1.3.2 Targeting strategies

Targeting strategies for nanoscale drug delivery systems can be divided in to two categories. Passive targeting takes advantage of certain unique features of the

tumor and its microenvironment for the selective delivery of agents to the tumor vasculature or cells. On the other hand, active targeting involves conjugating targeting components to nanoparticles in order to achieve preferential accumulation of nanoparticles at the tumor site.

Solid tumors have a diffusion-limited maximal size of about 2 mm^3 [14,15]. Angiogenesis enables tumor growth by granting them access to the circulation, but rapid vascularization to serve fast-growing cancerous tissues tends to result in leaky, defective architecture and impaired lymphatic drainage[16]. Matsumura *et al.*[17] first described an enhanced permeation and retention (EPR) effect due to this structure that allows nanoparticles to accumulate at the tumor site. Our group has previously established a relationship between probe size and tumor vessel permeability for relatively small macromolecules (3 - 10 nm) as well as estimated the pore cutoff size of the vessel wall to relatively large particles (100 - 2000 nm)[18,19]. EPR is a selective strategy that is now used in the clinic for particle-mediated delivery by liposomes[6,20]. For this passive targeting mechanism to work, the size and surface properties of the nanoparticles must be controlled to avoid uptake by the reticuloendothelial system (RES)[21].

It is now well known that a hydrophilic polymer coating, such as polyethylene glycol (PEG) increases circulation times of the nanoparticles, believed to result from decreased opsonization and subsequent clearance by macrophages in

addition to preventing plasma protein adsorption[22]. Our group and others have also demonstrated that cationic surface charge facilitates the accumulation of liposomes in the tumor vasculature[23-25].

Instead of relying on the EPR phenomenon, another method is the direct local delivery of anticancer agents to tumors. While this strategy is desirable because it circumvents the systemic circulation, direct administration is highly invasive as it involves injections and surgical procedures. In addition, some tumors, such as lung cancers, are difficult to access.

An alternative targeting strategy is to conjugate active recognition moieties to the surface of a nanoparticle. These targeting moieties provide preferential accumulation of nanoparticles in the tumor-bearing organ, tumor interstitium, individual cancer cells, intracellular organelles or specific molecules in cancer cells[3]. Employing molecularly targeted nanoparticles has several advantages over conventional antibody-guided therapy, including delivery of significantly greater therapeutic payloads per target biorecognition event, enhanced selectivity by carrying a cocktail of targeting agents, ability to integrate means to bypass biological barriers as well as the colocalized delivery of multiple agents, resulting in targeted combination therapy[2].

Although these targeting strategies are effective by themselves, synergistic combinations of these strategies will possibly achieve the greatest gain in therapeutic selectivity[2]. In the future, nanoscale vectors should serve as customizable, targeted drug-delivery vehicles capable of carrying large doses of anticancer agents into malignant cells while sparing healthy cells, thus reducing the damaging systemic responses to these drugs.

1.3.3 Quantum Dots

We now turn our focus to quantum dots (QDs) - colloidal semiconductor nanocrystals with unique photochemical and photophysical properties[26]. QDs used in biological imaging consist of an inorganic core, typically CdSe, that is the optically active center, an inorganic protective shell, typically ZnS, and an organic coating designed for biological compatibility and further conjugation (Figure 2). The cores are nearly spherical semiconductor nanoparticles, ranging from 2 - 10 nm in diameter.

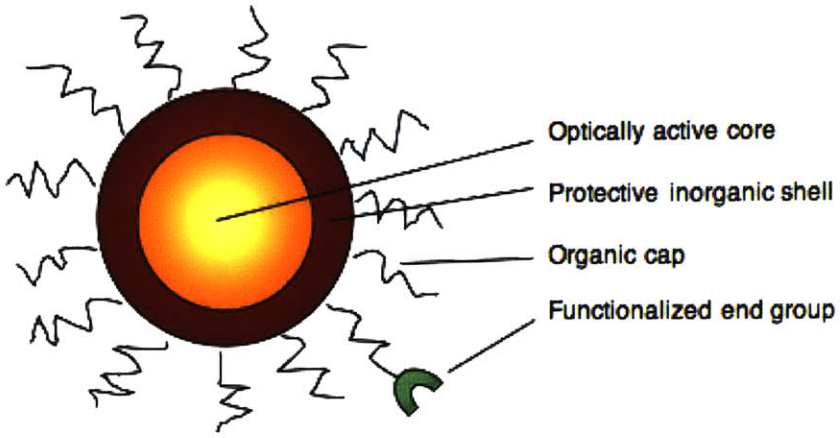

Figure 2. Schematic of a QD showing an optically active core, a protective inorganic shell an organic cap and one of the organic cap molecules functionalized.

These nanoparticles have several desirable properties that make them ideal for this study: they are several orders of magnitude brighter than conventional fluorophores, photostable, tunable to a desired narrow emission spectrum and relatively insensitive to the wavelength of excitation light[27]. Figure 3 shows the excitation and emission spectra for QDs of various colors.

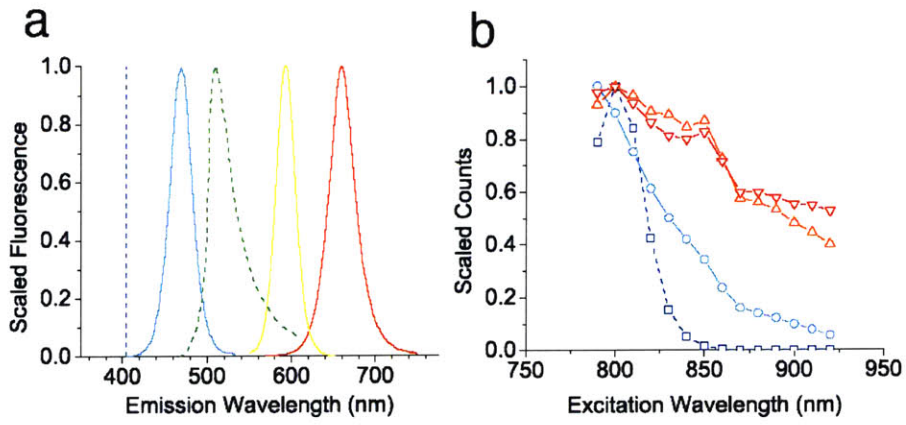

Figure 3. Quantum dot spectra. (a) QDs tuned to emit at wavelenghts not shared by signals from GFP and second harmonic generation with 810-nm incident light (green and dark blue lines, respectively). QDs exhibit a narrow and symmetric emission spectra (cyan, yellow and red lines).

(b) QDs have broad excitation spectra, as seen in the relatively broader two-photon action cross sections (cyan, orange and red lines) compared to cascade blue (dark blue line)

Robust water-soluble QDs have been created for biological applications such as multiphoton fluorescence imaging in live animals[27,28]. QDs have also been customized to distinguish multiple cellular components within the tumor milieu *in vivo* and to measure the ability of particles of different sizes to access the tumor[28]. Similarly, single particle tracking using a QD conjugated with tumor-targeting antibody has been performed to gain more insight on the interactions and processes involved in the transport of drug carriers in living mice[29].

Because QDs permit in vivo imaging at different length scales, it is also possible to image entire structures using QDs. Near infrared QDs have been successfully used to map lymphatic drainage and sentinel lymph nodes in mice and pigs[30,31]. Likewise, the macroscopic distribution *in vivo* of QDs can also be determined for studies on nonspecific uptake[32].

1.4 Tumor Interstitium

1.4.1 Barriers to Drug Delivery

In order to improve the delivery of therapeutics to solid tumors, it is crucial to understand the barriers to drug delivery and effectiveness. The first barrier any nanoparticle injected into the blood stream encounters is the chaotic blood supply of a tumor[5]. Unlike normal blood vessels, tumor blood flow is temporally and spatially heterogenous, resulting in compromised metabolic microenvironments and reduces then efficacy of certain therapies. The next barrier is the vessel wall, which is generally more permeable in tumors than in host tissues, but extremely heterogenous in permeability. Thus, nonuniform extravasation of nanoparticles occurs, leading to a spatial distribution that is heterogenous in the tumor.

Upon extravasation, the nanoparticles then face the challenge of moving through the interstitial space to reach the cancer cells. Transport of nanoparticles within the tumor interstitium depends on their size, charge and configuration, as well as the physico-chemical properties of the interstitium itself. The interstitium, is the third barrier and the focus of the remaining sections, which provides a summary of the tumor interstitial properties.

1.4.2 Composition of Tumor Interstitium

The interstitium is defined as the space located between the blood vessel wall and the cells. The basic structure of the interstitial space is similar in all tissue and is composed predominantly of a collagen fiber framework that contains a hydrophilic gel phase made up of glycosaminoglycans, a salt solution and plasma proteins[33]. The concentrations of collagen and hyaluronan (HA) content in human and murine tumors grown in mouse dorsal chambers measured by Netti *et al.*[34] are shown in Table 1. In general, the tumor interstitium is characterized by large interstitial space, high collagen concentration and low preteoglycan and HA concentrations[35]. Since the work of Gersh and Catchpole[36], the interstitium is often viewed as a two-phase system with a colloid-rich gel phase containing the hydrophilic hyaluronan (HA) and proteoglycans and a colloid-poor free fluid phase.

Table 1. Collagen and hyaluronan (HA) content in the interstitial matrix (IM) of human and murine tumors

Tumor Type	Collagen Content (mg/ml IM)	HA Content (mg/ml IM)
MCaIV (Mammary carcinoma)	9.0 ± 2.5	0.80 ± 0.15
LS174T (Human colon adenocarcinoma)	9.0 ± 2.5	0.55 ± 0.10
U87 (Human glioblastoma)	44.5 ± 21	0.55 ± 0.15
HSTS26T (Human soft tissue sarcoma)	29 ± 5.5	0.80 ± 0.10

1.4.2.1 Collagen and Elastin

The basic structural unit of the collagenous fibers is the collagen molecule (diameter, ~1.5 nm; length, ~300nm; molecular weight, ~285,000 kDa), formerly called tropocollagen[35]. The collagen molecule consists of three helical polypeptide chains (molecular weight, ~95,000 kDa) that are supercoiled to form a ropelike structure of great strength. At present, eleven different types of collagen are known and there may also be differences in the way the three polypeptide chains are assembled within each type. Nonetheless, each type has similar structure as a result of a repeating amino acid triplet, with every third amino acid being glycine[37].

Collagen is secreted from fibroblasts and the assembly of collagen molecules to form fibrils and subsequently fibers takes place extracellularly. Tumor collagen is produced by the host and its synthesis is governed by the tumor cells[38]. Not much is known about the control of thickness and orientation of collagen fibers, but it appears to be influenced by the presence of glycosaminoglycans[39,40]. Like other structural components of the interstitium, elastic fibers also have excluding properties. Nonetheless, since the elastin content in skin is only ~2% of wet weight[41], the absolute contribution from the elastic fibers to the total interstitial exclusion is small. Thus far, no attempt has been made to quantify the elastic fiber content of tumors.

1.4.2.2 Glycosaminoglycans

Glycosaminoglycans (GAG) are polyanionic polysaccharide chains of variable length made from repeating disaccharide units[37]. The disaccharide units have anionic groups (carboxylate-, sulfate ester- and sulfamino- groups) that are fully charged at physiological pH. Mutual repulsion of negative charges on the chains results in swelling in solution[35]. With the exception of hyaluronan, the seven subfamilies of GAG are bound covalently to a protein backbone and are known as proteoglycans[33]. Presently, data on proteoglycan content in tumors are limited[35].

Hyaluronan (HA, also called hyaluronic acid or hyaluronate) is a high molecular weight GAG (several million kDa) that is synthesized at and extruded through the plasma membranes of fibroblasts[42]. While the proteoglycans are immobilized in the interstitium, HA has not been shown to be immobilized[43]. HA is highly hydrophilic and each glucuronic acid unit contains one carboxyl group, giving rise to HA's polyanionic character at physiological pH[44]. In water, HA molecules can expand in volume up to 1000 times and form loose hydrated matrices. Thus, HA is thought to act as a space filler, lubricant and osmotic buffer[45].

1.4.3 Electrical Charge

As mentioned earlier, the GAG are negatively charged at physiological pH due to the substituted side groups on the sugar molecules, with one to three negative charges on each dissacharide unit. In the case of HA, Comper and Laurent measured a charge of -1 mol/mol HA-dissacharide unit (molecular weigh, 386 Da)[46]. On the other hand, collagen has a net positive charge at physiological pH. Li and Katz measured a charge of +14 mol/mol in reconstituted collagen[47]. The charge on collagen is less than that for HA on a molar basis, but could be of importance due to the large amount of collagen in the tumor interstitium. Overall, Wiig *et al.* suggested that the tumor interstitium acts as a negatively charged matrix[48]. The additional content of anionic proteoglycans perhaps causes the net negative interstitial charge observed.

1.4.4 Interstitial volume exclusion

The tumor interstitium is a crowded microenvironment and the presence of collagen and GAG limits the space accessible by plasma proteins and other macromolecules, a phenomenon called volume exclusion[49]. The main part of

exclusion has been attributed to the intrafibrillar space and the abundant collagen[50], but GAGs are also responsible for exclusion. In particular, HA, which has a very high exclusion per gram because of its random coil structure. The volume excluded per unit weight of native collagen has been estimated at 4 ml/g compared with 40 ml/g for HA[46,51]. The magnitude of the excluded volume has important consequences in the dynamics of transcapillary exchange. Furthermore, the presence of charged matrix components that are markedly increased during tumor development (such as HA) could potentially influence even further the tissue distribution of charged macromolecules via electrostatic repulsion forces[48].

1.4.5 Interstitial Transport

Transport of macromolecules within the tumor interstitium depends on their size, charge and configuration, as well as the physico-chemical properties of the interstitium itself. Since the interstitial fluid pressure in solid tumors is uniformly elevated, convection in the tumor interstitium is negligible[52] and the movement of macromolecules in the extracellular matrix (ECM) relies on passive diffusive transport[53].

1.4.5.1 Dependence on size, configuration charge and binding

Compared to normal tissue, the transport of macromolecules in tumor tissue is hindered to a lesser extent[54], which is consistent with reduced contents of GAGs and significantly larger interstitial spaces in tumors[55]. The effect of size/molecular weight on the diffusion of macromolecules in the tumor interstitium has been studied extensively[40,54,56,57] and interstitial diffusion has been shown to decrease with increasing molecular size. The effect of molecular configuration on diffusion in agarose gels[58] and microporous membranes[59] has also been investigated by comparing tracers with linear and globular configurations. Flexible macromolecules exhibited greater mobility in the gel than comparable-size rigid spherical particles, possibly due to trapping of the rigid particles in gel pores.

On the other hand, the effect of surface charge of macromolecules on their interstitial diffusion has not been studied extensively. In studies using charged agarose gels, Johnson *et al.*[60] reported that there were no effects of ionic strength on bovine serum albumin (BSA) diffusivities, but with smaller proteins there was a decrease in diffusivity at lowest ionic strength. Nugent *et al.*[54] found diffusive transport of BSA in the rat mesentery to be hindered more than dextran of same molecular size. Such a deviation could be explained by a smaller effective volume for diffusion due to electrostatic repulsion of negatively charged

albumin, in terms of configuration, or by the binding of BSA to tissue components. Thus, the effect of charge alone needs to be assessed in order to gain a better understanding.

1.4.5.2 Role of collagen and GAG

Diffusion of large molecules in tumors has been correlated to collagen content and organization, but not to HA content[34,40]. Specifically, collagen type I and its organization into fibrils is reported to play a significant role in limiting the diffusion of macromolecules. The narrow spacing between collagen fibrils (20-40nm) will exclude or hinder the migration of larger particles[40]. Nevertheless, Ramanujan *et al.*[61] suggested that unassembled collagen also plays a role in hindering diffusion after performing studies with collagen type I gels.

The alignment and spacing of collagen is modulated by proteoglycans[40]. However, it has yet to be determined if the interaction between proteoglycans and fibrillar collagen limits the diffusion of macromolecules in the interstitium. Similarly, the effect of HA on the diffusion of macromolecules is yet to be determined. HA solutions at concentrations comparable to several tumor types were shown to pose a weaker barrier to diffusion compared to that of collagen. Because hyaluronidase decreases diffusion of IgG in tumors[57], it is also possible

that the swelling potential of intact HA increases the pore size between ECM molecules and actually facilitates diffusion.

1.5 Conclusion

Nanotechnology is an emerging field that will potentially result in significant advances in early detection, molecular imaging, assessment of therapeutic efficacy, targeted and multifunctional therapeutics as well as the prevention and control of cancer. Despite the promise of nanotechnology for a bright future, nanosized hybrid therapeutics and drug delivery systems will not be advantageous unless they reach the desired target in effective concentrations. In general, the tumor interstitium is characterized by large interstitial space, high collagen concentration and low proteoglycan and HA concentrations. Modification of the net charge of a nanoscale vector in order to assess its effect on transport in tumors is an important investigative tool in cancer therapy. Recently, a powerful technique - fluorescence correlation spectroscopy (FCS) was optimized for *in vivo* measurements of diffusion of macromolecules in tumors and revealed the two-phase nature of transport[57]. The emergence of FCS as a new and highly sensitive method to probe interstitial transport parameters

could potentially shed new light on our understanding of the transport phenomena in the tumor interstitium.

Chapter 2: Fluorescence Correlation Spectroscopy

2.1 Introduction

Fluorescence correlation spectroscopy (FCS) is an experimental technique that uses statistical analysis of the fluctuations of fluorescence in a system in order to study kinetic processes. FCS was first introduced more than 30 years ago to measure diffusion and chemical kinetics of DNA-drug intercalation[62,63]. This extremely powerful and sensitive technique has since been applied to measure translational diffusion, rotational diffusion, flow and chemical reactions [63-66].

Even when a system is at equilibrium, its components are continually fluctuating about their thermodynamic mean concentration. If the observed region of the solution is open, these fluctuations are caused by random variations in the number of molecules that enter or leave the region by diffusion and by the molecules that are formed or eliminated by chemical reactions. Observation of these spontaneous fluctuations can yield a complete kinetic description of the system[63]. In order to measure the number of molecules of a specific type in a defined open volume of solution as a function of time, the molecules can be fluorescently labeled and their emitted fluorescence intensity, which is

proportional to the number of fluorescing molecules in the illuminated region, is monitored over time. If the number of molecules in the illuminated volume is small enough, fluorescence fluctuations due to the diffusion of molecules in and out of the volume becomes measurable. It is not possible to determine diffusion coefficients accurately from the time courses of single stochastic fluctuations, so a large number of fluctuations need to be measured and analyzed statistically[67]. The fluctuations can be quantified in their strength and duration by temporally autocorrelating the recorded intensity signal, providing a measure of self-similarity of the intensity signal and thus describing the persistence of information carried by it. In other words, the fluorescence fluctuation autocorrelation function yields the rate at which the fluctuations dissipate (rate of relaxation of the system to equilibrium), averaged over many fluctuations[68].

Early measurements suffered from poor signal-to-noise ratios, mainly due to the low detection efficiency, large ensemble numbers and insufficient background suppression. The basic problem was that experimentally measurable fluctuations in fluorescence intensity occur only for very small sample volumes. For one-photon excitation, lasers can be focused to submicron beam waists in the radial dimensions, but there is no confinement along the beam axis. Because of such limitations, early applications of FCS were restricted to two-dimensional systems[69].

However, the application of confocal microscopy techniques to FCS successfully solved the volume problem[70,71]. On the other hand, multiphoton FCS provides a superior alternative to confocal FCS by achieving even higher signal-to-noise ratios, reduced autofluorescence and photobleaching as well as improved penetration in turbid media[69,72]. These advancements, coupled with the incorporation of avalanche photodiode (APD) and photomultiplier tubes with high photon quantum efficiency have enabled FCS studies to be conducted in gels[73], living cells[72], and more recently, living animals[57].

2.2 Theory of FCS

FCS is performed on samples maintained at thermal equilibrium so that all of the processes under analysis are in fact statistical fluctuations around equilibrium. The kinetic coefficients corresponding to these processes such as diffusion coefficients determine the dynamics of their relaxation, which in turn determines the shape of the fluorescence fluctuation correlation curve. The presentation of the theory of FCS in this section follows closely the line and notation of Schwille and Haustein[74] with some minor modifications introduced.

The normalized fluorescence fluctuation autocorrelation function is defined as:

$$G(\tau) = \frac{\langle \delta F(t)\, \delta F(t+\tau) \rangle}{\langle F(t) \rangle^2} \qquad (1)$$

where $\delta F(t)$ represents the fluorescence fluctuations resulting from whatever process is occurring in an open ensemble of molecules of an average concentration $\langle C \rangle$ in a detection volume V, illuminated by focused laser light.

The fluorescence emitted by the molecules in the focal spot is recorded photon-by-photon and assuming constant excitation power, the fluctuations of the fluorescence signal are defined as deviations from the temporal average signal:

$$\delta F(t) = F(t) - \langle F(t) \rangle \qquad (2)$$

$$\langle F(t) \rangle = \frac{1}{T} \int_0^T F(t)\, dt \qquad (3)$$

If all fluctuations arise only from changes in the local concentration within the effective volume of the focal spot, the variations can be written as:

$$\delta F(t) = \kappa \langle I_0 \rangle \int_V S(\underline{r})\, Q(\underline{r})\, \delta\big(\sigma q C(\underline{r},t)\big)\, dV \qquad (4)$$

In the above equation, κ represents the overall detection efficiency of the optical system comprising of collection optics, filters and detectors, q is the fluorescence quantum yield of the dye, σ is the molecular absorption cross-section, and C denotes the local particle concentration. $\langle I_0 \rangle$ is the average intensity at the geometrical focal point and $S(\underline{r})$ is the dimensionless spatial distribution

function of the focused light in the sample space. $Q(\underline{r})$ is the collection efficiency function weighting factor for confocal optics.

To simplify equation 4, the convolution factor of the two dimensionless spatial optical transfer functions can be combined into a single function, $W(\underline{r}) = S(\underline{r}) * Q(\underline{r})$ which describes the spatial distribution of the emitted light. $W(\underline{r})$ can be approximated as a three-dimensional Gaussian, which is decayed to $1/e^2$ at r_0 in the lateral direction and at z_0 in the axial direction.

$$W(\underline{r}) = e^{-2\left(x^2+y^2/r_0^2\right)} e^{-2\left(z^2/z_0^2\right)} \tag{5}$$

The remaining parameters $\langle I_0 \rangle, \sigma$, κ and q can be combined into a parameter, η, that describes the photon count rate per detected molecule per second. This parameter is also used as a measure for the signal-to-noise ratio of the measurement.

$$\eta = \kappa \langle I_0 \rangle \sigma q \tag{6}$$

Substituting (5) and (6) into (2), we now have:

$$\delta F(t) = \int_V W(\underline{r})\, \delta(\eta C(\underline{r},t))\, dV \tag{7}$$

Now we insert (7) into (1) to obtain:

$$G(\tau) = \frac{\iint W(\underline{r}) W(\underline{r}') \langle \delta(\eta C(\underline{r},t)) \delta(\eta C(\underline{r}', t+\tau)) \rangle \, dV \, dV'}{\left(\int W(\underline{r}) \langle \delta(\eta C(\underline{r},t)) \rangle \, dV \right)^2} \tag{8}$$

The fluctuation term $\delta(\eta C(\underline{r},t)) = C\delta\eta + \eta\delta C$ can be simplified assuming the chromophore's fluorescence properties are not changing within the observation time, i.e., $\delta\eta = 0$, resulting in:

$$G(\tau) = \frac{\iint W(\underline{r})W(\underline{r}')\langle\delta(C(\underline{r},0))\delta(C(\underline{r}',\tau))\rangle\, dV\, dV'}{\left(\langle C\rangle \int W(\underline{r})\, dV\right)^2} \tag{9}$$

If we only consider particles that are freely diffusing in three dimensions with the diffusion coefficient D, the number density autocorrelation term can be calculated:

$$\langle\delta(C(\underline{r},0))\delta(C(\underline{r}',\tau))\rangle = \langle C\rangle(4\pi D\tau)^{\frac{3}{2}} e^{-\frac{(\underline{r}-\underline{r}')^2}{4D\tau}} \tag{10}$$

Inserting (10) into (9) yields:

$$G(\tau) = \frac{1}{\langle C\rangle(4\pi D\tau)^{-\frac{3}{2}}} \frac{\iint W(\underline{r})W(\underline{r}')e^{-\frac{(\underline{r}-\underline{r}')^2}{4D\tau}}\, dV\, dV'}{\left(\int W(\underline{r})\, dV\right)^2} \tag{11}$$

Finally, substituting (5) into (11) results in the expression for the normalized three-dimensional diffusion autocorrelation function for one species of molecules:

$$G(\tau) = \frac{1}{V_{eff}\langle C\rangle}\left(1+\frac{\tau}{\tau_D}\right)^{-1}\left(1+\frac{\tau}{K^2\tau_D}\right)^{-\frac{1}{2}} \tag{12}$$

In the above equation, V_{eff} is defined as the effective focal volume:

$$V_{eff} = \frac{\left(\int W(\underline{r})\, dV\right)^2}{\int W^2(\underline{r})\, dV} = \frac{\left(\int e^{-2\left(x^2+y^2/r_0^2\right)} e^{-2\left(z^2/z_0^2\right)} dV\right)^2}{\int e^{-4\left(x^2+y^2/r_0^2\right)} e^{-4\left(z^2/z_0^2\right)} dV} = \pi^{\frac{3}{2}} r_0^2 z_0 \tag{13}$$

τ_D, the average lateral diffusion time for a molecule with diffusion coefficient D through the effective measurement volume element V_{eff} is defined as:

$$\tau_D = \frac{r_0^2}{4D} \tag{14}$$

From equation (12) we can see that it is possible to determine the local concentration of fluorescent molecules from the amplitude of the autocorrelation curve, $G(0)$:

$$G(0) = \frac{1}{V_{eff}\langle C \rangle} = \frac{1}{\langle N \rangle} \tag{15}$$

Because the amplitude of the autocorrelation function is inversely proportional to the average number of molecules in the focal volume, it is important to minimize the concentration of fluorescent molecules to obtain a better correlation signal. Typically, the temporal average of the particle number should be between 0.1 and 1000, which corresponds to concentrations between sub-nanomolar ($<10^{-9}$ M) and micromolar (10^{-6} M) for a focal volume around one femtoliter. Alternatively, decreasing the size of the focal volume can increase the amplitude.

2.3 Multiphoton FCS (MPFCS)

In this thesis, the term muliphoton excitation (MPE) refers primarily to a two-photon excitation (TPE) event. The advantage MPE offers to FCS is the natural 3D localization of the excitation volume inherent in nonlinear excitation. In the case of TPE, the intensity-squared dependence is the basis of the localized nature of two-photon excitation: doubling the intensity produces four times the fluorescence[75].

Using a three-dimensional Gaussian function to describe the dimensions of the MPE focal volume allows for derivation of simple analytic expressions for the lateral $1/e$ radius ω_{xy} as well as the axial $1/e$ radius, ω_z[75].

$$\omega_{xy} = \begin{cases} \dfrac{0.32\lambda}{\sqrt{2}\,NA} & NA \le 0.7 \\ \dfrac{0.325\lambda}{\sqrt{2}\,NA^{0.91}} & NA > 0.7 \end{cases} \tag{16}$$

$$\omega_z = \frac{0.532\lambda}{\sqrt{m}} \left[\frac{1}{n_i - \sqrt{n_i^2 - NA^2}} \right] \tag{17}$$

where m is the excitation order (e.g., m=2 for TPE) and n_i is the index of refraction of the immersion media. Conversion to $1/e^2$ radii, r_0 and z_0, can be obtained by multiplication by $\sqrt{2}$.

The equations in this section only hold true for diffraction-limited optics. This refers to when the objective lens entrance pupil (back aperture) is overfilled. In

practice, this requires that the $1/e$ diameter of the beam be at least equal to the entrance of the pupil diameter[76].

For MPFCS, several changes need to be made to equations 13 and 14. Integrating the three-dimensional Gaussian yields[72,75]:

$$V_{eff} = \pi^{3/2}\omega_{xy}^2\omega_z = \left(\frac{\pi}{2}\right)^{3/2} r_0^2 z_0 \qquad (18)$$

The above volume approximation is 0.68 of the value calculated by numerical integration of the two-photon illumination spread function[77], so equation 18 should be further multiplied by 1.47 for the best approximation of the effective excitation volume.

The average lateral diffusion time for MPFCS, τ_D, is also slightly different due to the introduction of the convolution factor as a squared instead of a simple Gaussian[72].

$$\tau_D = \frac{r_0^{\,2}}{8D} \qquad (19)$$

Chapter 3: Instrumentation Development for Multiphoton Fluorescence Correlation Spectroscopy

3.1 Introduction

The previous chapter described in detail the theory of FCS and the advantages of multiphoton excitation (MPE). Here, we describe the experimental realization of MPFCS. Our setup was designed to enable diffusion measurements of nanoparticles to be carried out in gel models of the tumor interstitium as well as in live animals.

MPFCS can be implemented using the same scheme for two-photon laser scanning microscopy invented by Denk[78] *et al.* By integrating MPFCS with our home-built multiphoton laser scanning microscope (MPLSM), the specimen can be imaged with the same illumination and excitation optics. Thus, we can image the nanoparticle distribution, examine collagen structure and content, as well as measure the diffusion coefficients of the nanoparticles.

3.2 Experimental realization of MPFCS

3.2.1 Optical and hardware setup

In our setup (Figure 4), pulsed laser light from a Mai Tai femto-second titanium-sapphire (Ti:S) laser (Spectra Physics) is first expanded by a factor of 2 in order to overfill the back aperture of a high power objective that is used to focus the light inside the sample. The X-Y scanner (a modified Fluoview scanhead BX61W1 from Olympus) allows images of the sample to be taken and once a spot is chosen for diffusion measurements, the laser beam is parked at the desired location. Since the probability of a two-photon event is extremely low, all of the absorption occurs only in a small region near the focus where the energy density is the highest. Fluorescence emission from the excitation volume is focused into a GaAsP photomultiplier tube (PMT) after passing through a bandpass filter to select the emission spectra of interest. Fluctuations in fluorescence intensity are recorded as fluctuations in the photocurrent of the PMT exposed to fluorescent radiation and a digital correlator card performs autocorrelation of the fluorescence intensity signal. The resulting autocorrelation curve is displayed on a computer that allows control of data acquisition time and analysis of the autocorrelation curves.

Since photon counting is required for FCS, detectors with high quantum efficiencies must be used. Avalanche photodiodes are commonly used in FCS setups because of their high quantum efficiencies, but the small active area of an APD makes alignment more difficult then necessary. As an alternative, the detector we chose to use is a GaAsP PMT (Hamamatsu H7421-40) that has a spectral response from 300 - 720 nm, a 5x5 mm active area and about 42% quantum efficiency at 550 nm.

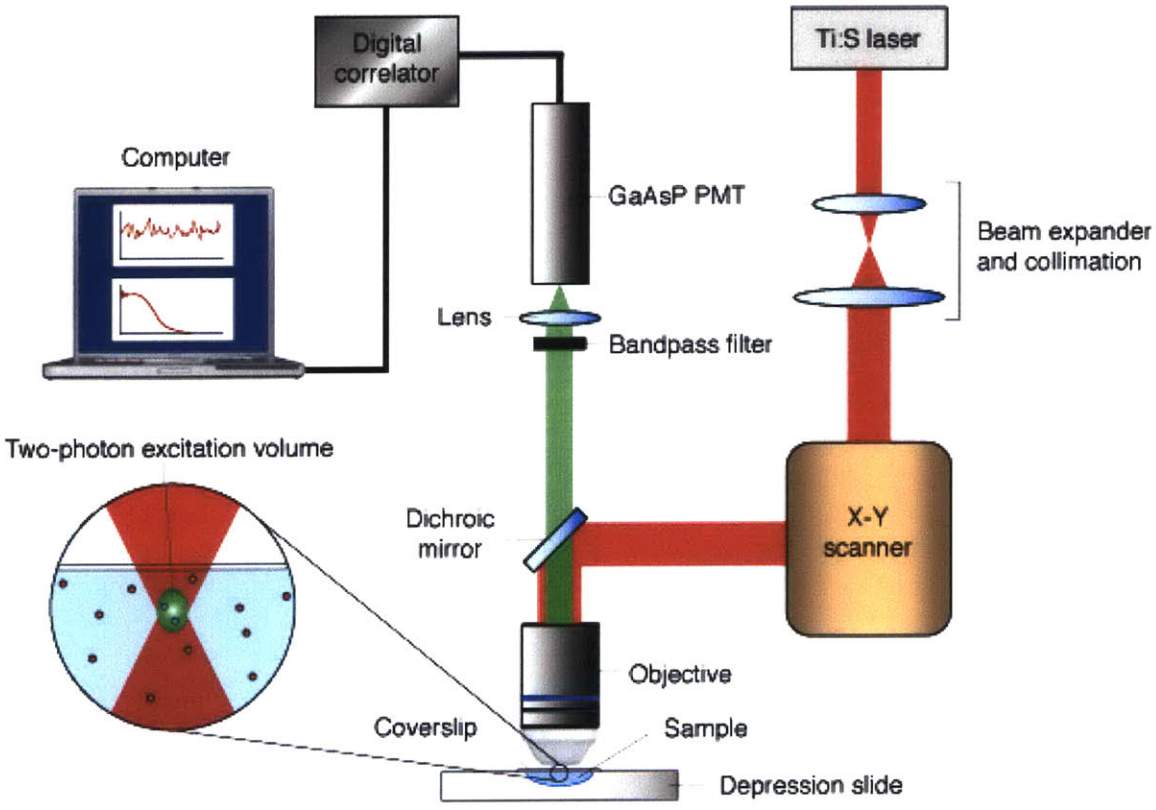

Figure 4. Optical setup for MPFCS measurements. Laser light (red) is expanded, collimated and focused by a high power objective inside the sample. Fluorescence (green) emitted by excited molecules within the two-photon excitation volume is collected and focused into a PMT with single-photon sensitivity.

For the best collection of fluorescence, it is also important to use high power objectives with larger numerical apertures (NAs). Originally, a Olympus 20x 0.95 NA water immersion lens was selected because of its high NA and wide field of view. However, the expanded laser beam diameter was limited by the size of the X-Y scan mirrors and could not overfill the large back aperture of this particular lens (17 mm). Thus, FCS measurements were carried out using an Olympus 63x 1.2 NA water immersion lens instead.

Autocorrelation curves were generated using a digital correlator card in order to provide almost real-time visualization of the quality of the FCS measurements. The USB based hardware correlator (Flex 012-12D, Correlator.com) continuously counts the number of photons in a short time period and increments the lag time in the autocorrelation calculation in a logarithmic fashion in order to cover several orders of magnitude (nanoseconds to a few seconds).

3.2.2 Software for data analysis

In order to extract information from the autocorrelation curves, we developed software to analyze the raw data and perform data fitting in MATLAB. First, the software extracts the intensity history and correlation functions from the output of the digital correlator card and stores them in vectors. Using a nonlinear least

squares fitting routine, the correlation functions are then fitted to a model specified by the user. Available models include single component free diffusion, multicomponent free diffusion (2 - 3 components), anomalous diffusion and anisotropic diffusion. In addition, models that accounted for triplet state kinetics were also included. For all models, the values for r_0 and K were fixed, with the exception of a calibration model for focal volume size determination. Users also can specify upper and lower bounds to the free parameters in order to improve the resulting fits by including more information. Upon completion of a fit, the software then plots the experimental data and resulting fit on a graph as well as returns the fit parameters along with the goodness of fit measurements.

As the amount of data to process increased, the software was also improved to allow for batch processing. An entire dataset can be analyzed and the extracted fit values are exported as a text file while the set of figures are exported as a postscript file.

3.3 Calibration of MPFCS system

3.3.1 Testing the digital correlator card

One of the first components to be tested was the Flex012-B digital correlator card. In order to do so, a function generator was used to provide periodic input signals of various frequencies. The output of the digital correlator when square waves and sine waves of different frequencies were applied showed peaks at the respective periods of the input signal. This is exactly what we expect since periodic signals will produce peaks in their autocorrelation function when the overlap is maximum, i.e. at every time period. Thus, we confirmed that the digital correlator card was indeed working.

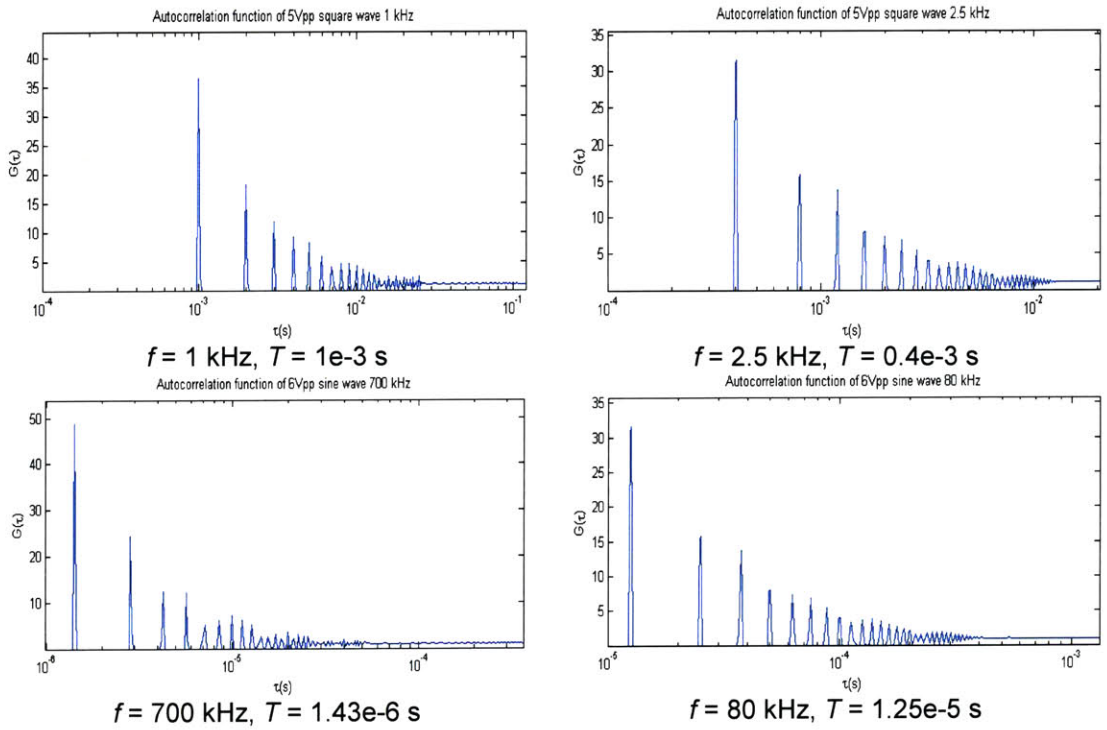

Figure 5. Testing the digital correlator card. Square waves and sine waves with 5V peak-to-peak voltages were generated at different frequencies and the output of the correlator card recorded. The autocorrelation curves produced show peaks at every time period, T, corresponding to the frequency, f, of the input signal.

3.3.2 Measurement of laser power at sample

The relationship between the laser power measured before entering the X-Y scanbox and at the sample was examined for the 60x, 1.2 NA objective (Olympus). From Figure 6, we see that the laser power at the sample is around 7 times less than the laser power measured before entering the scanbox. This can be attributed to the power loss at the lenses and mirrors, as well as the objective lens.

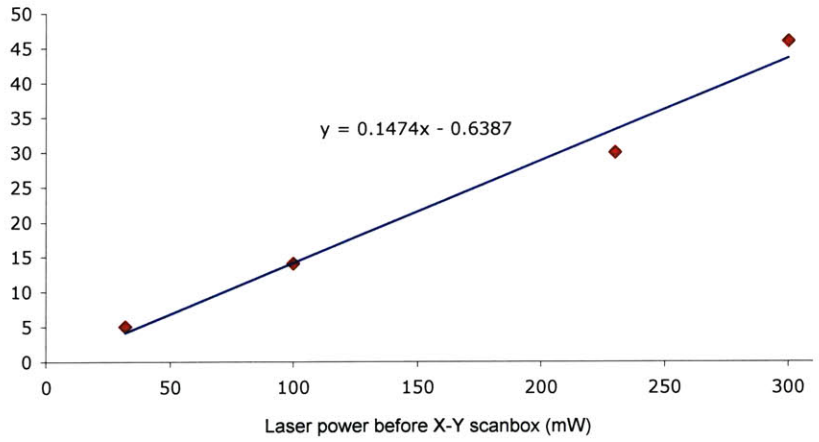

Figure 6. Relationship between laser power before X-Y scanbox and laser power at sample. Laser power at the two locations were measured for 4 different settings (red diamonds) and a linear best fit line (blue line) yields the relationship between the two.

3.3.3 Testing the stability of MPFCS setup

Because FCS is such a sensitive technique, the stability of the optical setup is very important to ensure accurate measurements. To minimize the effect of floor vibrations, the MPFCS setup was built on a vibration isolation optical tabletop. In addition, the X-Y scanner has to be stable so that when the laser is parked, it will not introduce artifacts into the data due to the residual motion or vibration of the galvanometers.

To test for our system's stability, we performed FCS measurements of fluorescently labeled beads stuck on a microscope slide. Autocorrelation curves of green fluorescent microspheres (1 μm diameter, Polysciences Inc.) and red fluoresecent microspheres (Polymer microspheres, 0.25 μm diameter, Invitrogen) dried on slides are shown in Figure 7.

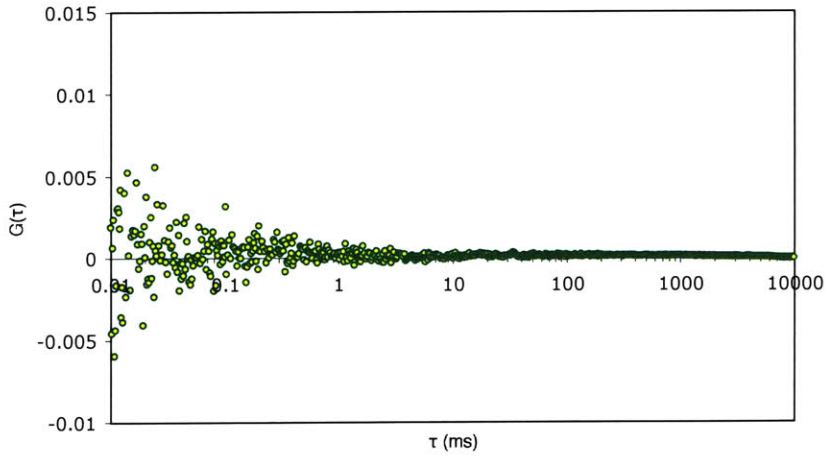

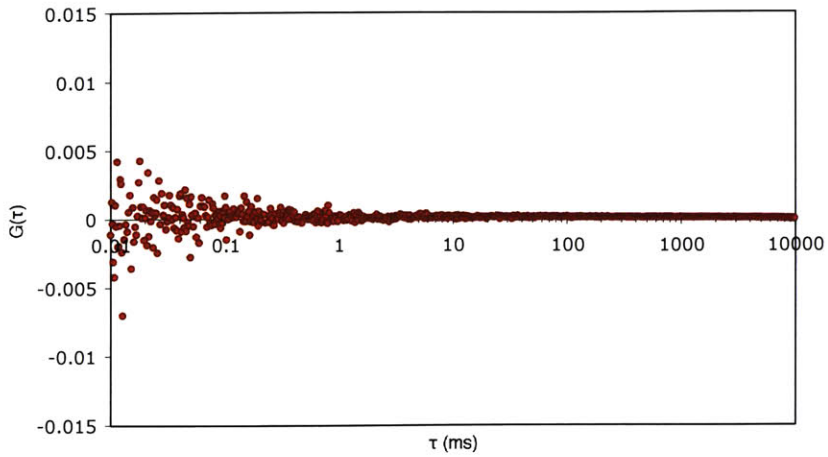

Figure 7. Test for stability of MPFCS system. Autocorrelation curves of 1 µm (yellow-green) and 0.28 µm (red) fluorescent microspheres stuck on a microscope slide display a flat profile. FCS measurements were performed at 800nm excitation and with 2.9 mW laser power at sample.

Since there is no movement of the fluorescent microspheres in and out of the excitation volume, there is no correlation function (flat profile). Fluctuations in fluorescence intensity in this situation are due mainly to shot noise which is random and does not produce a correlation, since fluctuations at different time intervals are not correlated. If there were others sources of non-random fluctuations, correlation would be present in the curves shown above.

3.3.4 Characterization of the excitation volume

The effective focal volume, V_{eff} and the $1/e^2$ values in the lateral (r_0) and axial (z_0) direction can be estimated experimentally by calibration of the system with a dye of known dynamic properties. The data analysis is slightly different when

characterizing the focal volume. Instead of having the diffusion coefficient, D, set as a free variable, D is fixed to a known value while r_0 and the aspect ratio, K are allowed to vary freely.

The objective characterize was an Olympus 60x (1.2 NA) water immersion lens with a correction collar. Since it has been suggested that the correction collar can eliminate spherical aberrations for a wide range of beam collimations to yield an asymptotic minimum focal volume[79], we perform an experiment varying the correction collar setting for each FCS measurement to determine its effect on the focal volume (Figure 8).

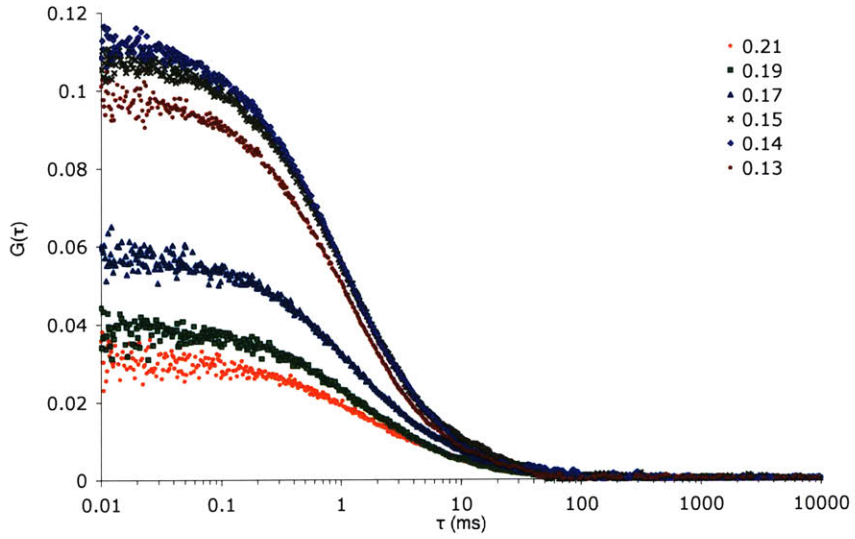

Figure 8. Effect of correction collar setting on autocorrelation functions. FCS measurements were performed on fluorescent microspheres in solution at 800 nm excitation with constant laser power at the sample (2.9 mW) and different correction collar settings.

It is clear that the amplitude of the autocorrelation functions, $G(0)$, decreases as the correction collar setting increases. From equation (15), we know that $G(0)$ is inversely proportional to the effective focal volume. Thus, we can use the inverse of $G(0)$ as an indicator of the focal volume size to find the optimum collar setting (Figure 9).

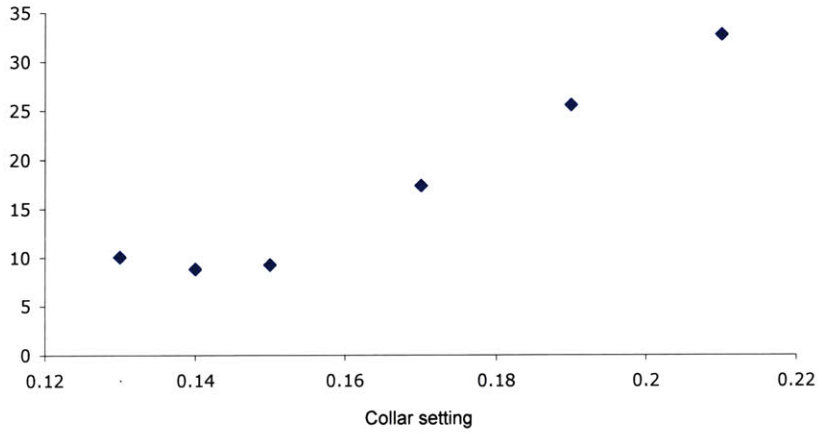

Figure 9. Relationship between focal volume size and correction collar setting. The focal volume size increases as collar setting increases and its minimum value is around 0.14.

Since the focal volume size increased with higher correction collar setting, the laser beam in our system could be slightly diverging[79] and not perfectly collimated. In any case, the optimum collar setting was 0.14 to achieve the minimum focal volume and was fixed for all remaining experiments.

We chose to use a sample of red fluorescent microspheres (Duke Scientific) in with a mean hydrodynamic diameter of 0.28 μm to characterize the focal volume

of our MPFCS system. For a spherical particle of radius r, its diffusion coefficient can be calculated using the Stokes-Einstein equation:

$$D = \frac{k_B T}{6\pi\eta r} \tag{20}$$

In the equation above, k_B represents the Boltzmann's constant, T is absolute temperature and η is the viscosity of the medium. Thus, using equation (20), we estimated the diffusion coefficient of the 0.28 μm microsphere to be 1.7507 x 10^{-7} cm^2/s in water at room temperature. With this information, analysis of FCS measurements of the microspheres in solution (Figure 10) yielded r_0 = 0.36 μm and K = 5.

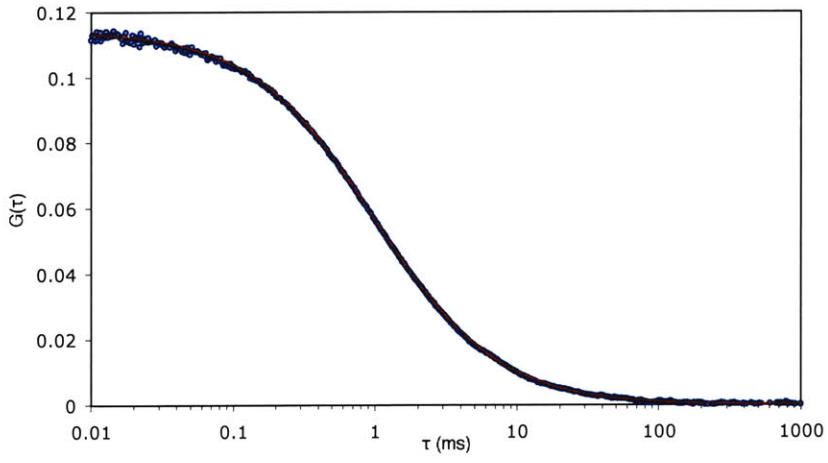

Figure 10. Calibration of focal volume size. FCS measurements (blue circles) were performed on a sample of 0.28 μm microspheres in distilled water at 800 nm excitation and 2.9 mW laser power at the sample. A total of five measurements were performed (each 60s long) and averaged before fitting (red line) for r_0 and K with D fixed at 1.7507x10^{-7} cm^2/s.

Typically, rhodamine-6G is used for calibration because it has a well know diffusion coefficient of 2.8 x 10^{-6} cm^2/s in solution at room temperature[62].

However, measurements are not easily obtained because the size of rhodamine-6G approaches the resolution limit of our MPFCS system and the laser power at the sample needs to be very low (< 3 mW) to avoid saturating or photobleaching the dye. Furthermore, since rhodamine-6G sticks to the walls of the slide and to the bottom of the coverslip, the slides and coverslips must be coated with nonfluorescent BSA prior to sample preparation. Using our estimated values of r_0 and K, measurements of rhodamine-6G (Figure 11) yielded D = 2.721 x 10^{-6} cm^2/s, which is in good agreement with literature.

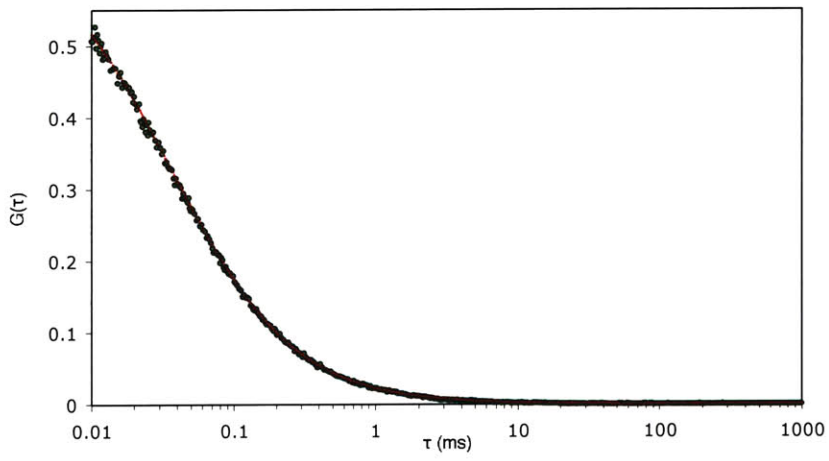

Figure 11. Diffusion of rhodamine-6G in solution. FCS measurements (green circles) were performed on nM concentration of rhodamine-6G in distilled water at 800 nm excitation and 2.9 mW laser power at the sample. A total of ten measurements (each 120s long) were performed and averaged before fitting (red line) to yield D = 2.721 x 10^{-6} cm^2/s.

Theoretical estimates of the focal volume produced by a 1.2 NA objective with 800 nm excitation light using equations (16) and (17) yield r_0 = 0.22 μm and K = 2.6 , which is significantly smaller than the values determined experimentally. These values are unreliable because Gaussian beam theory assumes uniform

overfill of the back aperture and perfect beam collimation, which in practice, is extremely difficult to achieve. In addition, high NA objectives may not have ideal modulation transfer functions from manufacturing due to strong attenuation of marginal rays[80].

3.3.5 FCS measurements in solution

Further calibration of the MPFCS system was performed by measuring the diffusion of size series of microspheres (Polysciences, Inc.) in solution. For each size, the theoretical diffusion coefficient was calculated using equation (20) and compared to the values obtained by FCS (Figure 12). Our measurements matched the predictions by the Stokes-Einstein equation very closely, demonstrating the accuracy of our system.

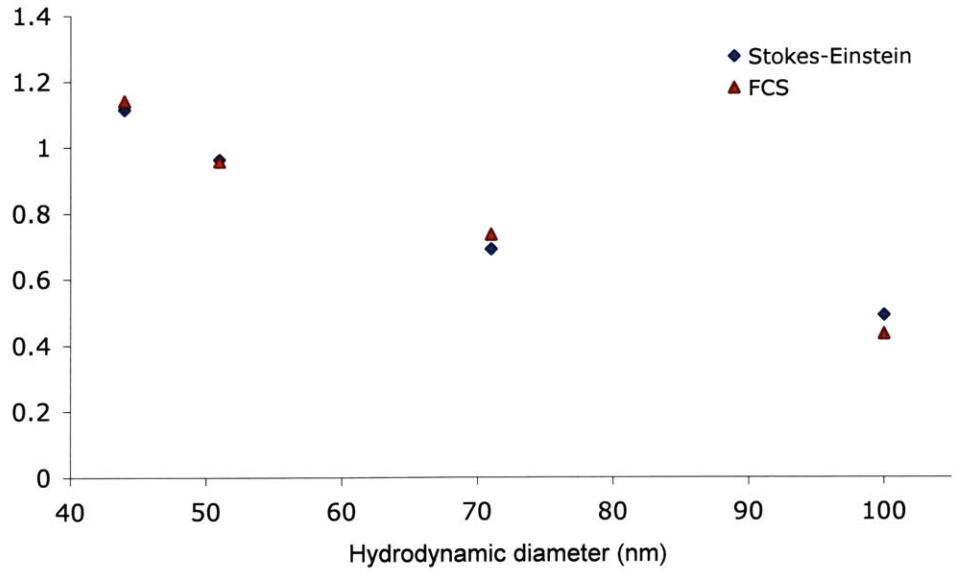

Figure 12. FCS performed on a size series of microspheres. Diffusion measurements (red triangles) were performed for microspheres of different sizes (44, 51, 71, 100 nm) in distilled water at 800 nm excitation and 3.6 mW laser power at the sample. Ten measurements (each 15 – 60s) were performed for each different microsphere. Theoretical values (purple diamond) are shown for comparison.

We also measured the diffusion of tetramethylrhodamine-conjugated albumin (TAMRA-BSA) using our system. Once again, the value we obtained (D = 6.462 x 10^{-7} cm^2/s) agreed with literature value of 6.4 x 10^{-7} cm^2/s [81].

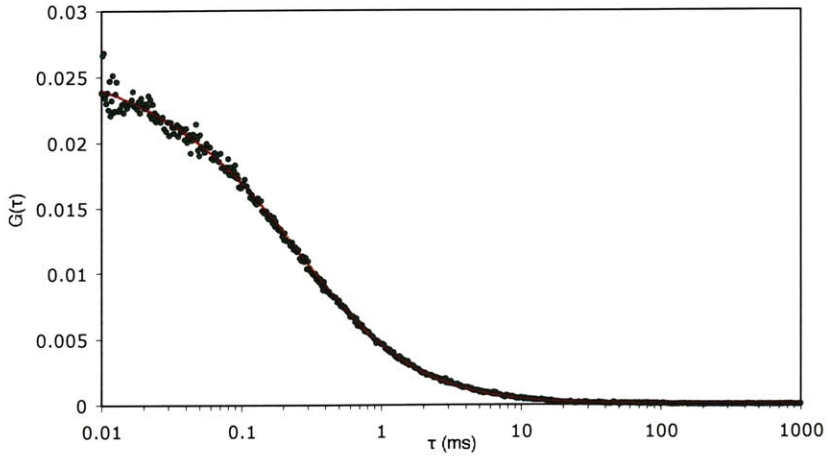

Figure 13. Diffusion of albumin in solution. FCS measurements (green circles) were performed on TAMRA-BSA in distilled water at 800 nm excitation and 2.9 mW laser power at the sample. A total of ten measurements (each 120s long) were performed and averaged before fitting (red line) to yield $D = 6.462 \times 10^{-6}$ cm^2/s.

3.3.6 Characterization of the field of view

Finally, we characterized the field of view (FOV) for two different objective lenses under MPE (20x Olympus 0.95 NA and 60x Olympus 1.2 NA) using a stage micrometer (Graticules Ltd) that has 100 separate divisions with 10 μm per division.

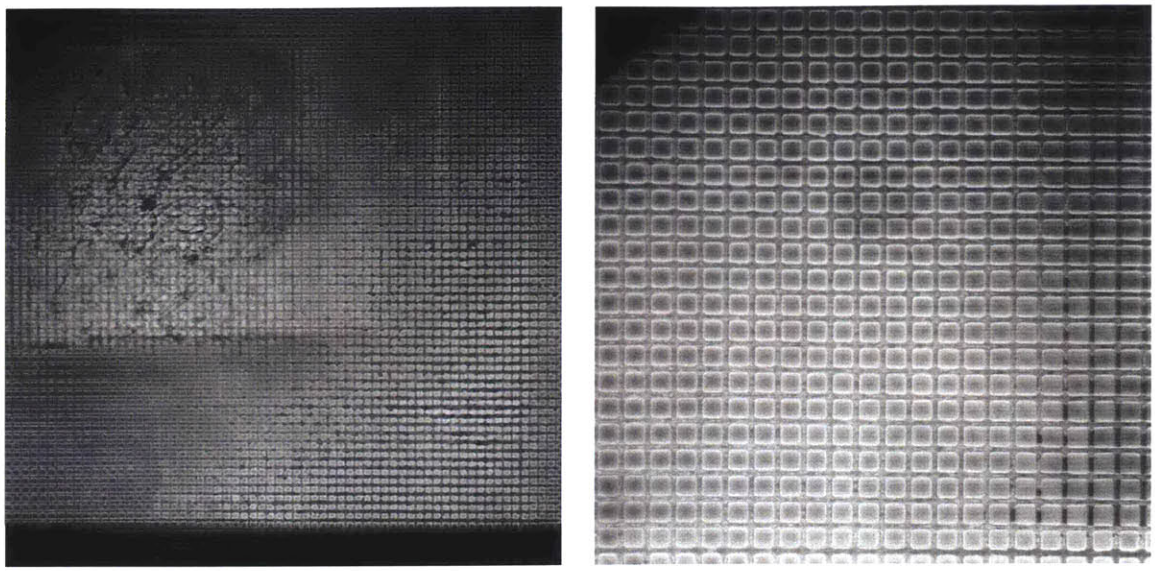

Figure 14. Field of view characterization. Images of a stage micrometer taken with an Olympus 20x 0.95 NA (left) and Olympus 60x 1.2 NA (right). Divisions are 10 μm apart. Image sizes are 1024 x 1024 pixels.

Analysis of Figure 14 showed that the FOV for the Olympus 20x 0.95 NA objective is 630 x 630 μm and the FOV for the Olympus 60x 1.2 NA objective is 223 x 223 μm.

Chapter 4: Fluorescence Correlation Spectroscopy of Quantum Dots

4.1 Motivation

As highlighted in Chapter 1, the tumor interstitium is a barrier to drug delivery and modification of the net charge of a nanoscale vector in order to assess its effect on transport in tumors is an important investigative tool in cancer therapy. Nonetheless, the biological complexity of the tumor interstitium makes detailed analysis of the mechanisms of transport hindrance within the tumor difficult. Such problems can be overcome by performing studies in gel models of the tumor matrix as diffusion data in gels have been reported to closely match *in vivo* measurements[61].

In this chapter, we report the results of MPFCS diffusion measurements of charged QD nanocrystals in collagen gels and collagen-HA composite gels. In addition, we present MPLSM images of QD distribution and SHG images of collagen organization inside the two gel models.

4.2 Characterization of QDs

Our collaborators from the Bawendi Lab at MIT prepared QDs of three different charges by modifying the surface of pre-made CdSe/CdZnS QDs with dihydrolipoic acid (DHLA), DHLA-polyethyleneglycol (DHLA-PEG) and amino-functionalized DHLA-PEG (DHLA-PEG-NH_2). The chemical structures of these molecules are shown in Figure 15.

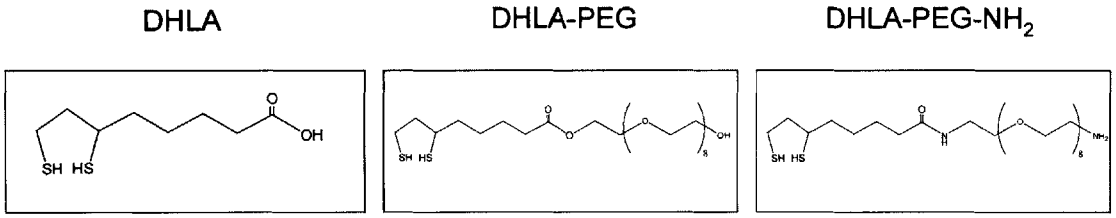

Figure 15. Chemical structures of molecules used to modify QD surface charges. DHLA was selected to provide a negative charge, DHLA-PEG provides a "neutral" charge and DHLA-PEG-NH_2 provides a positive charge.

Before any valid comparisons between the diffusion of QDs with different surface charges can be made, it is important to characterize their physicochemical properties. Thus, the size of the QD samples after surface modification was measured to ensure that the three samples had similar sizes. Measurements of the hydrodynamic radius for each QD sample were performed using dynamic light scattering (DLS). The zeta-potential of the each different QD sample, which is the electrostatic potential generated by the accumulation of ions at their surface was also determined (Brookhaven ZetaPALS). The measured size

and charge of each of the QD samples are reported in Table 2 to compare the different modification strategies.

Table 2. Physicochemical properties of QD samples

Sample	Hydrodynamic radius (nm)	Zeta-potential (mV)
QD-DHLA-PEG-NH_2	5.83	37.39
QD-DHLA-PEG	6.2	-18.16
QD-DHLA	5.37	-31.12

The hydrodynamic radii of all three samples were similar even after surface modification, but the zeta-potential indicated all three samples had a different charge associated. The emission spectra of the QD samples were also measured and the emission peak was around 640 - 650 nm.

4.3 MPFCS of QDs in solution

Before measuring the diffusion of the QDs in solution, we imaged the samples in PBS to examine the monodispersity of each sample. For all experiments, QD samples were passed through 0.1 μm pore size filters to remove aggregates and diluted to final concentrations around 20 nM. Artifacts of FCS have been reported due to blinking and saturation effects of QDs[82], thus we investigated the shape of QD FCS curves as a function of laser excitation power. Final FCS

measurements for the three QD samples were obtained using the optimal power that exhibited no artifacts and produced a good signal-to-noise ratio.

4.3.1 Results and discussion

4.3.1.1 Distribution of QDs in solution

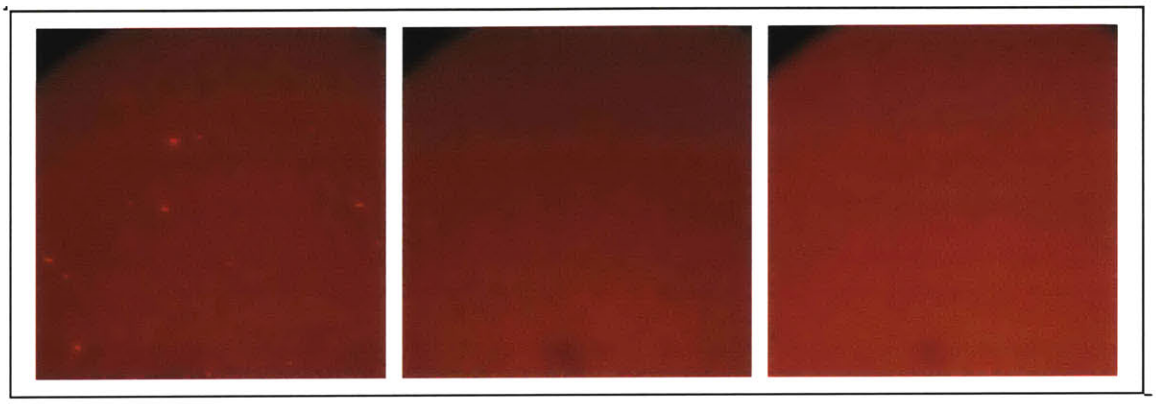

Figure 16 depicts the distribution of three QD samples in PBS obtained by MPLSM. The images indicate the all QD samples were uniformly distributed in solution and did not exhibit aggregation with the exception of small agglomerates in the QD-DHLA-PEG-NH_2 sample.

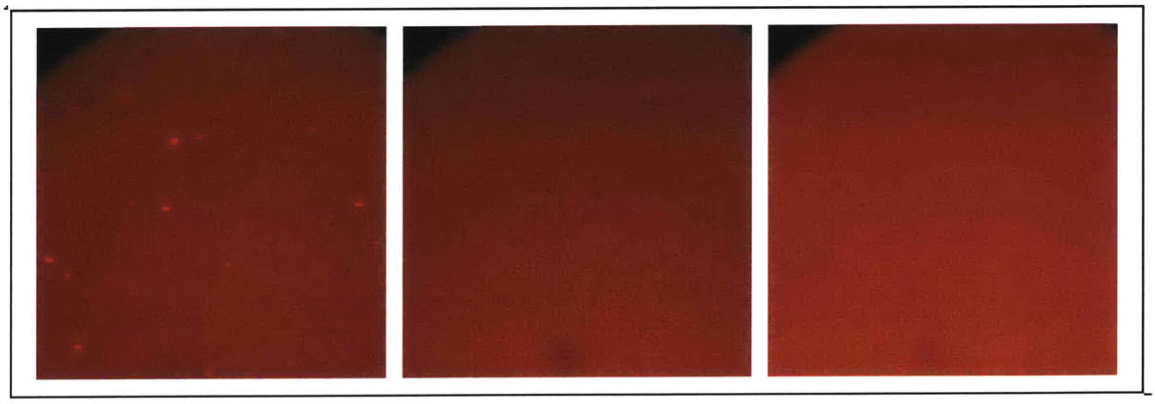

Figure 16. Images of QD-nanocrystals (Emission max: 650 nm) in phosphate buffer solution (1x PBS) using MPLSM. The distribution of QD nanocrystals (red) modified with DHLA-PEG-NH_2 (A), DHLA-PEG (B), and DHLA (C) are shown in PBS. Images are 223 μm across.

4.3.1.2 Curve shape variations

We found that the shape of the autocorrelation curves highly depended on the laser excitation power, as shown in Figure 17. The decrease in $G(0)$ as the laser power increases is in agreement with reports in literature[73,82].

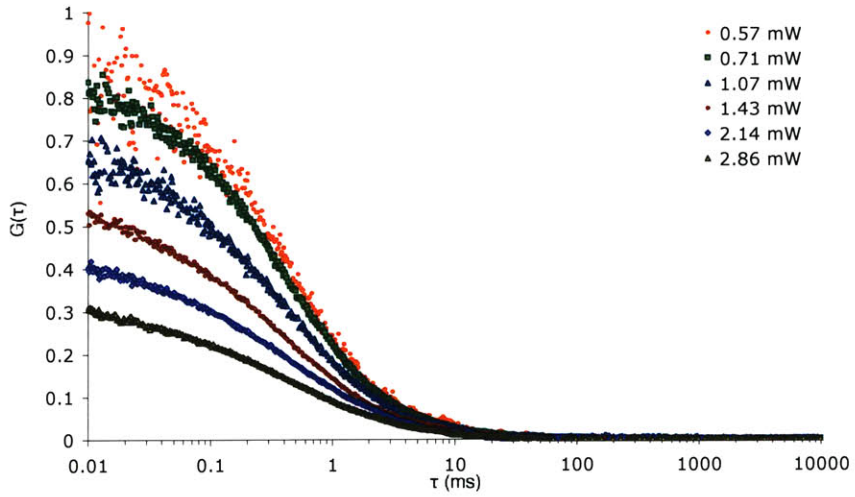

Figure 17. Typical FCS curves for QDs recorded at various excitation powers. The amplitude decreases visibly with increasing powers.

One of the reasons could be due to excitation saturation of QDs, illustrated in Figure 18. Above a certain laser intensity, the probability of exciting a fluorescent particle at the center of the focal volume approaches unity. When the fluorescent particle at the center are saturated, their emitted fluorescence is no longer proportional to the laser intensity (in the case of TPE, emitted fluorescence is proportional to intensity squared). As a result, when the laser power is further increased, the fluorescence emission intensity from the center of the focal volume no longer grows proportionally with the edges, leading to an effective point spread function (PSF) that looks like a top-hat and its effective size (the full width at half maximum, FWHM) is increased. Recalling equation (15), an increase in V_{eff} will result in a decrease of $G(0)$.

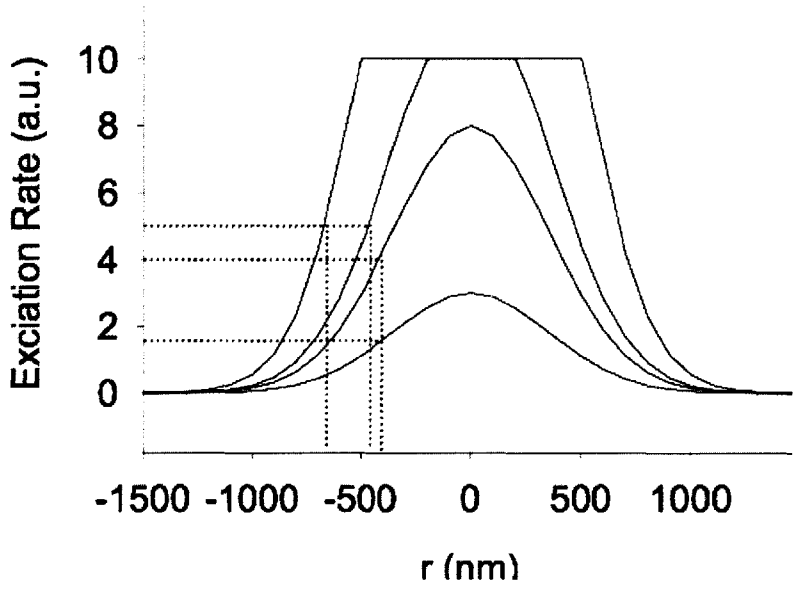

Figure 18. Excitation rate profile of a fluorescent particle as a function of position and laser excitation power. As laser power is increased, the top of the Gaussian profile is clipped and starts to look like a top-hat, thereby increasing the effective focal volume.

Heterogeneity in QD emission properties has also been suggested and QDs have been reported to exhibit blinking (fluorescence intermittency)[83]. Since blinking statistics of individual QDs change with excitation power, the changes in FCS curves as a function of excitation power could also reflect modifications in blinking parameters[82]. Nonetheless, Larson *et al.* found no evidence for temporal fluctuations other than molecular diffusion when performing FCS measurements on QDs at low excitation powers[27]. Thus, we chose to operate at below 0.71 mW to reduce the possibility of QD blinking corrupting FCS measurements.

4.1.1.1 Diffusion in solution

Experimental data obtained for QDs modified with different end groups are shown in Figure 19. Because no analytical expression to fit FCS curves can be derived as of now, we fitted the curves with a simple single component diffusion model (equation 12).

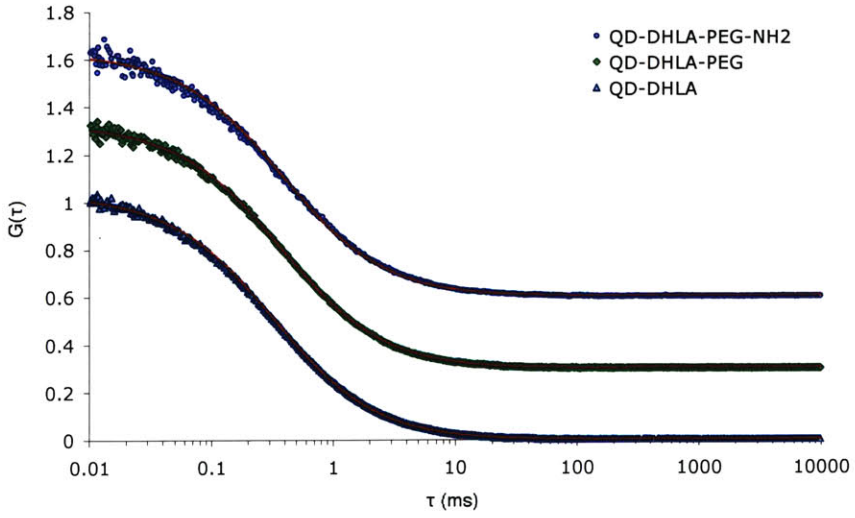

Figure 19. FCS curves of QDs with different surface modifications. Experimental data was fitted to a single component free diffusion model (red lines). At least five measurements were taken for

each sample at laser powers between 0.4-0.7 mW at the sample. Offset between curves for presentation purposes is 0.3.

The extracted diffusion coefficients and corresponding hydrodynamic radii are shown in Table 3. Our results match well with the reported DLS measurements, albeit indicating that the QDs are slightly smaller in size. Nonetheless, the difference in diffusion coefficients between samples is not large, suggesting that size will not be a major factor when evaluating their transport in gels.

Table 3. Diffusion coefficients and size of QD samples. The error is the standard deviation derived from different measurements.

Sample	D ($\times 10^{-7}$ cm^2/s)	Hydrodynamic radius (nm)
QD-DHLA-PEG-NH_2	4.24 ± 0.07	5.78 ± 0.11
QD-DHLA-PEG	4.38 ± 0.08	5.60 ± 0.10
QD-DHLA	5.02 ± 0.15	4.89 ± 0.15

4.4 MPFCS of QDs in gels

4.4.1 Methods

Collagen hydrogels were polymerized by mixing the following components in order on ice: 97.7 µl 9.37 mg/ml acid-soluble rat tail tendon collagen (BD Biosciences) and 2.3 µl of sodium hydroxide (1 N). After vortexing, QD samples were introduced and the mixture was immediately pipetted onto coverglasses

that were subsequently sealed in petri dishes with a drop of water at the edge (Fisher). The samples were then incubated for 1 hour at 37 °C. Final concentration of collagen was 9.15 mg/ml.

Collagen-HA composite gels were prepared in the exact same manner with the additional step of mixing 20 μl of 3 mg/ml hyaluronan after the collagen was neutralized with sodium hydroxide. Final concentration of collagen was 7.63 mg/ml and HA was at 0.5 mg/ml. These concentrations closely matched the reported values for LS174T (Table 1).

After the incubation period, coverslips containing the gel samples were sealed in depression slides (VWR Scientific) and MPFCS measurements were performed at room temperature. For each QD type, three gels were used to determine the diffusion coefficient. Images of QD distribution within gels were taken with MPLSM and the collagen structure was visualized using second harmonic generation (SHG).

4.4.2 Results and discussion

4.4.2.1 Organization of gels

The structure and organization of gels visualized by SHG is shown in

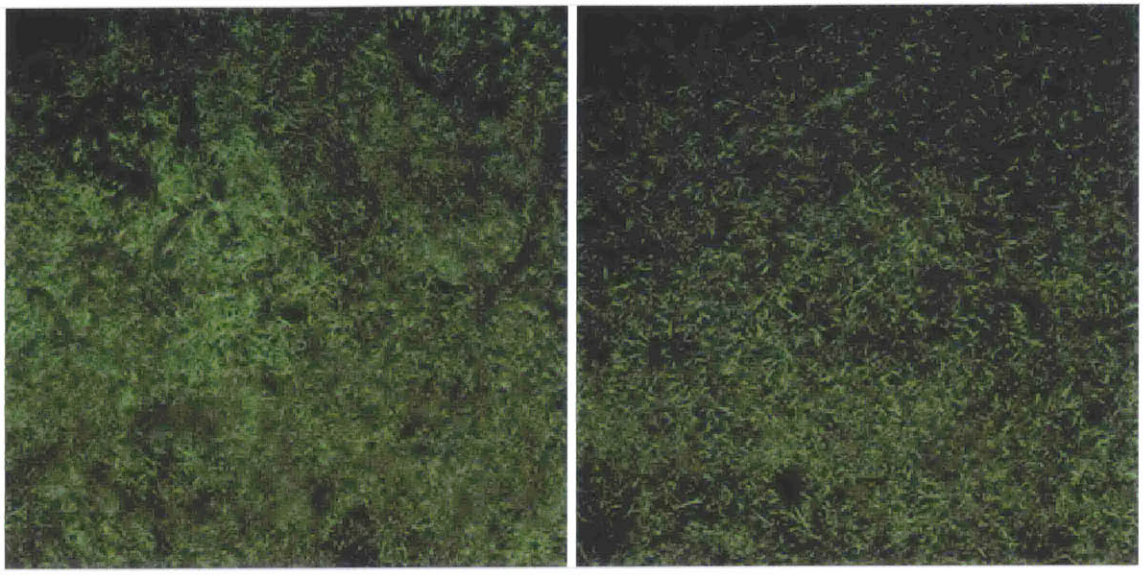

Figure 20.

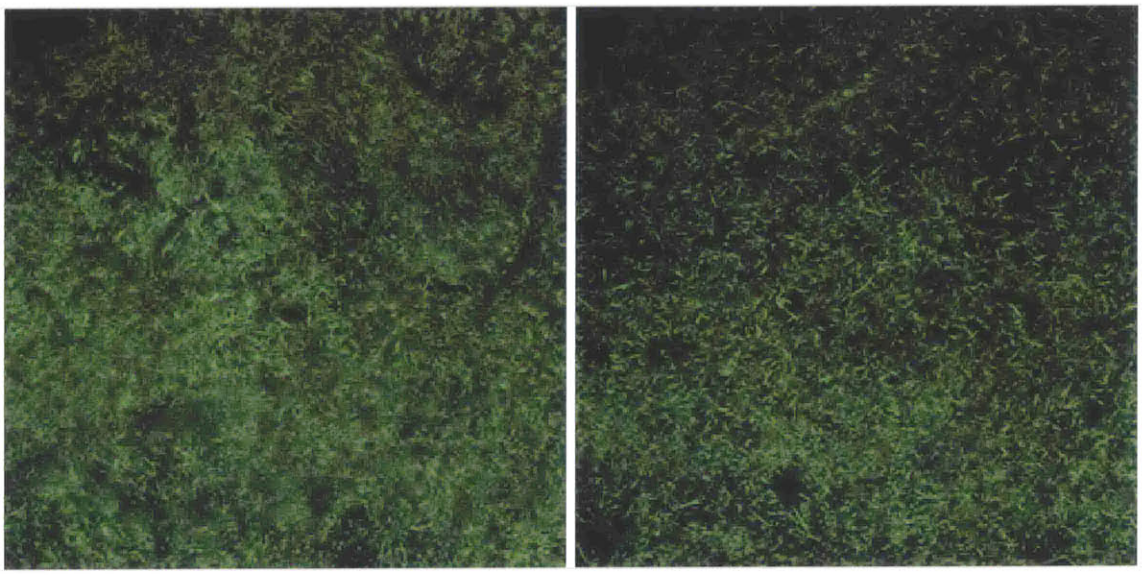

Figure 20. Organization of gels. SHG images of collagen gels (left) and collagen-HA composite gels (right) reveal inhomogeneous organization and short, dense fibers. Images are 223 across.

The gels appear to be isotropic and three-dimensional in nature while the organization of collagen is poor with dense arrays of short fibers. The inhomogeneous organization of collagen is in agreement with previous studies

in our lab[61]. The fibers in the pure collagen gel appeared to be a little denser than those in the composite gel, possibly due to the slightly higher concentration of collagen. Three-dimensional reconstruction confirmed the three-dimensional nature of collagen gels (Figure 21). We did not have the resolution in our imaging techniques to measure the average pore sizes of the gels. In addition, since SHG only visualizes fibrillar collagen, our data does not rule out the existence of unpolymerized collagen in what appears to be void spaces.

Figure 21. Three-dimensional rendering of collagen gel. 86 images were reconstructed, revealing three-dimensional nature of collagen organization. Dimensions are 223 x 223 x 50 μm.

4.4.2.2 Distribution of QDs in gels

Distribution of QDs within the network of collagen gels and collagen-HA composite gels are shown in Figure 22 and Figure 23 respectively. In both gel types, QD-DHLA (anionic) appeared to have form large agglomerates within the fiber network and this is especially evident in the collagen gel (Figure 22-G) .The presence of cationic QD-DHLA-PEG-NH_2 aggregates can also be seen in the collagen-HA composite gels (Figure 23-A), but no large agglomerates are seen in the collagen gels (Figure 22-A). Nonetheless, the distribution of the cationic QDs within the collagen gels is not entirely homogenous, with what appears to be void spaces visible. In both gel types, the distribution of neutral QD-DHLA-PEG is uniform across the entire gel.

The significant differences in distribution for QDs of difference surface charges suggest that the electrostatic interactions might be an important factor in determining the distribution of nanoparticles. Electrostatic repulsion of like charges could cause QDs to form aggregates, but it is unclear how binding due to opposite charge attaction can lead to aggregation. The stability of surface modified QDs during the gelation phase at 37°C is also questionable, but the difference observed between the cationic QDs in different gel types and the homogeneous distribution of neutral QDs in both gels seem to suggest that temperature is not the cause of the aggregation. Regardless, we can conclude that QD-DHLA-PEG provides the best distribution across both gels. This could potentially lead to significant improvements in drug delivery.

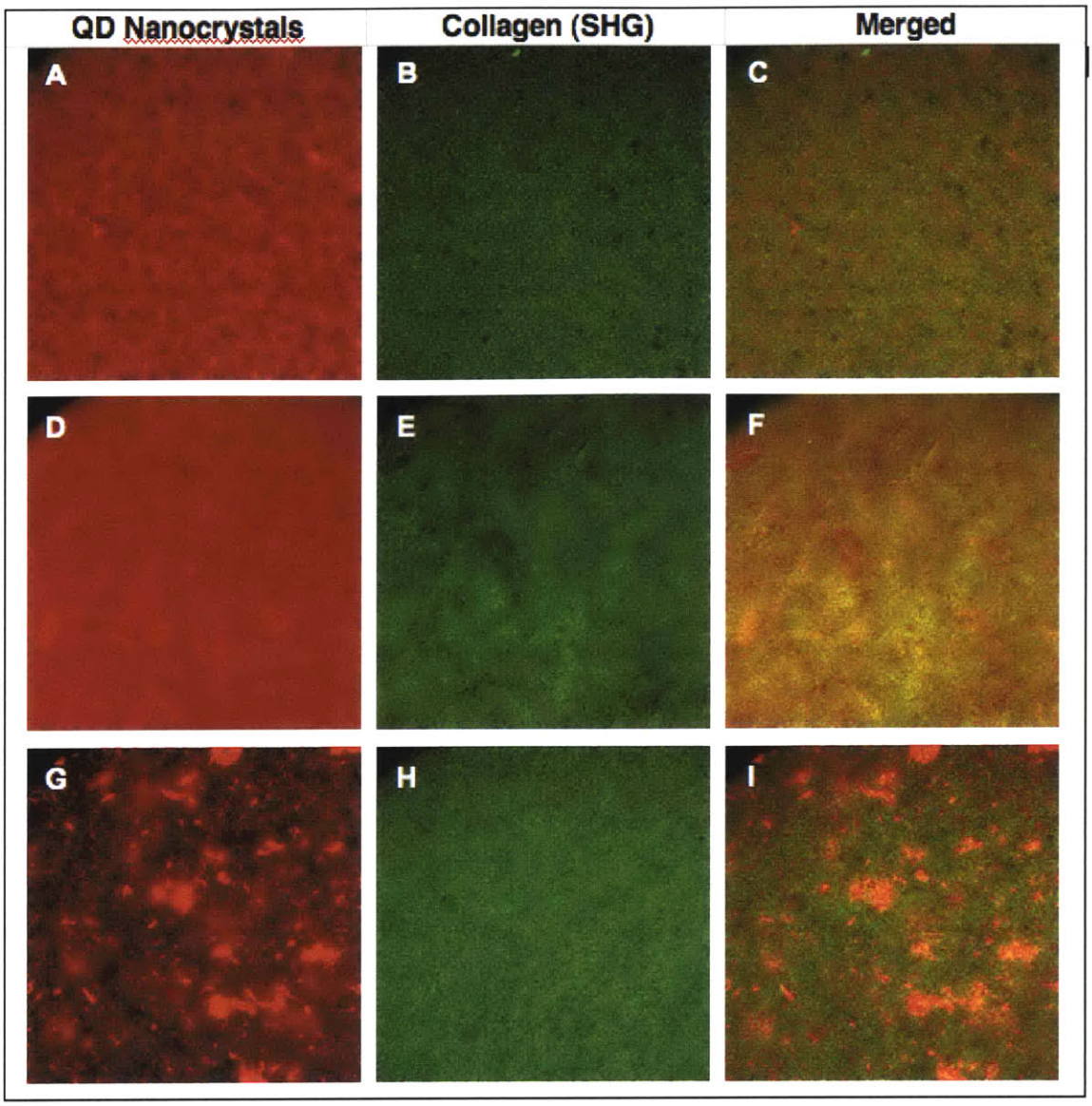

Figure 22. Images of QD-nanocrystals in **collagen** gels using multiphoton microscopy. Distribution of QD nanocrystals (red) modified with DHLA-PEG-NH_2 (A-C), DHLA-PEG (D-F), and DHLA (G-I) are shown in gels composed of collagen type I fibers (green). Images are 630 μm across.

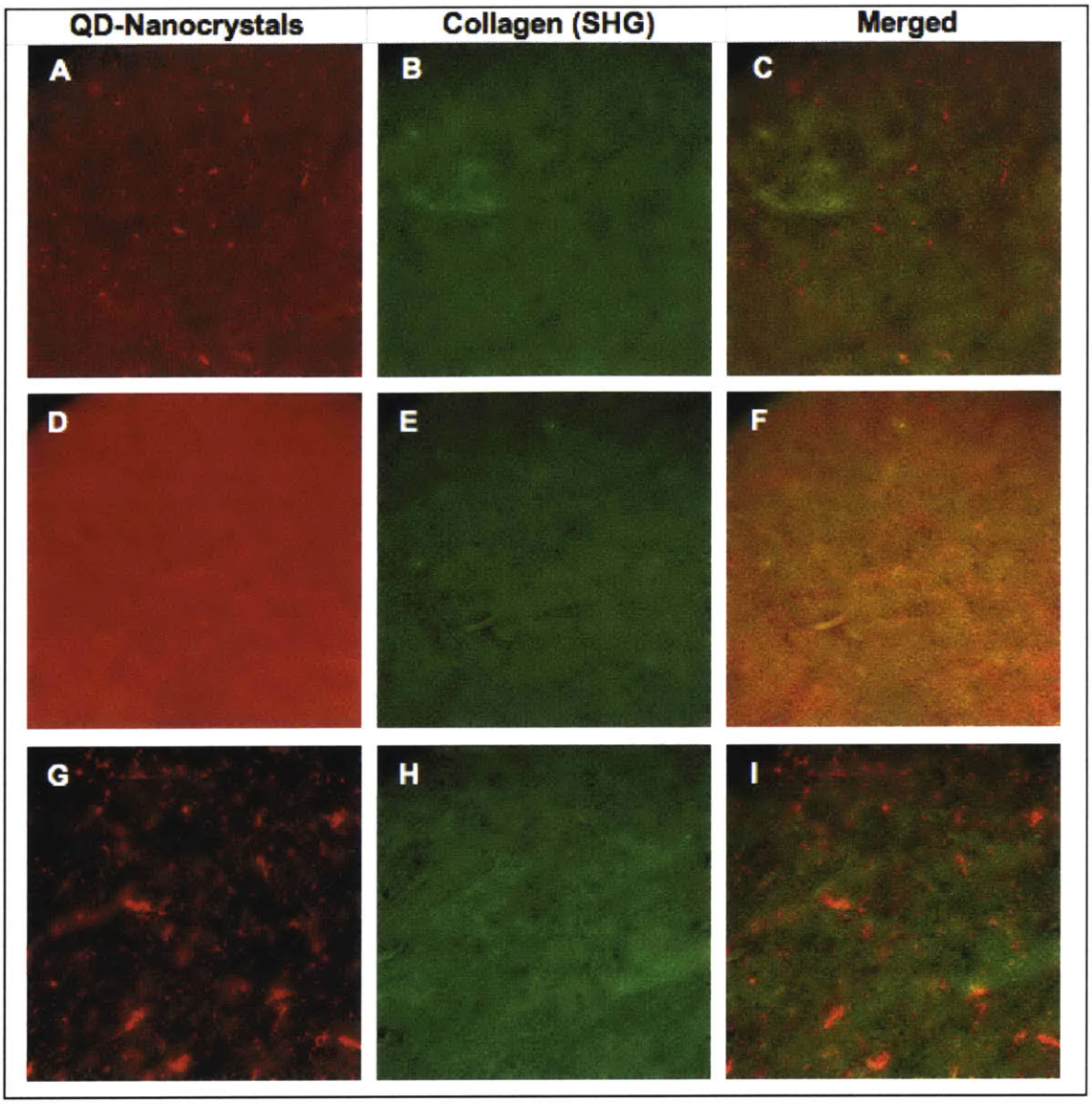

Figure 23. Images of QD-nanocrystals in **collagen-HA** composite gels using multiphoton microscopy. Distribution of QD nanocrystals (red) modified with DHLA-PEG-NH_2 (A-C), DHLA-PEG (D-F), and DHLA (G-I) are shown in gels composed of collagen type I fibers (green). Images are 630 μm across.

4.4.2.3 Transport of QDs in gels

QDs in both gels exhibited a photo-brightening effect in which their fluorescence emitted increased over time when excited by a parked pulsed laser. Because of this unusual phenomenon, FCS measurements had to be made in short time intervals (20s) so that the intensity fluctuations had a constant mean value within those short intervals. Furthermore, FCS measurements could not be performed everywhere in the gels except spots with low concentration and free of aggregation. FCS curves obtained by measuring the diffusion of QDs in both collagen gels and collagen-HA composite gels could not be described by a single component free diffusion equation (**Error! Reference source not found.**). We fitted the experimental data to a variety of other models and found that our data can be described in two different ways.

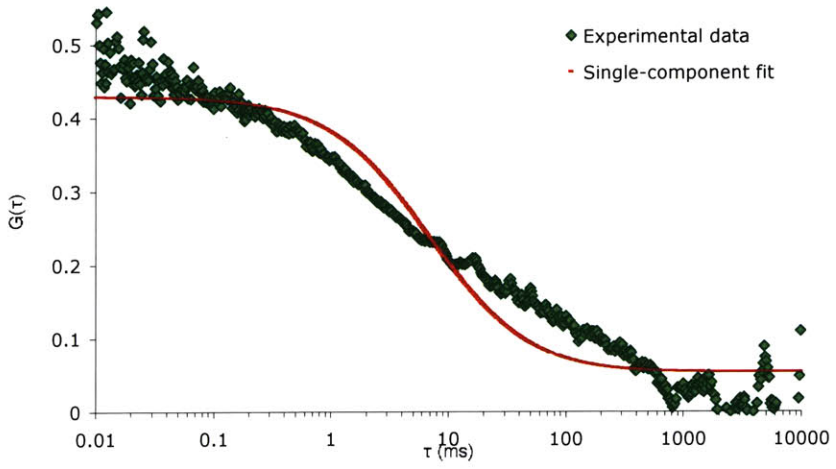

Figure 24. Typical FCS curve of QD diffusion in gels. A 20s measurement of QD-DHLA-PEG in collagen-HA composite gel was obtained at 800 nm excitation and with 0.7 mW laser power at

sample. A single component free diffusion model (equation 12) produced a poor fit for the experimental data.

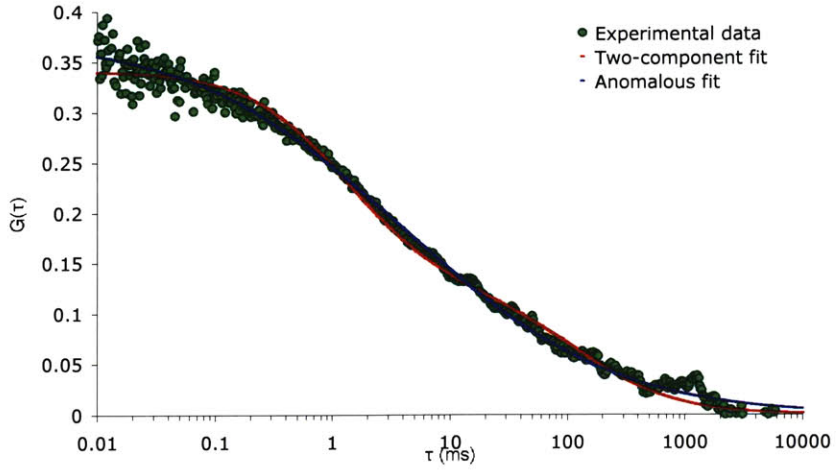

Figure 25. FCS data of QD transport in gels described by anomalous subdiffusion and two-component free diffusion. Anomalous diffusion (purple) and two-component (red) models provided good fits for experimental data.

The first model describes anomalous subdiffusion, a case in which diffusion is hindered and the mean square displacement, $\langle r^2 \rangle$, is no longer linear but proportional to some power of time < 1:

$$\langle r^2 \rangle = 8\Gamma t^{\alpha} \tag{21}$$

In the equation above, α is the temporal exponent and lies between 0 and 1, and Γ is the transport coefficient of fractional time dimension. Anomalous diffusion is simply a generalization of simple diffusion (which occurs when α = 1) and equation 12 is modified by replacing $\frac{\tau}{\tau_D}$ with $\left(\frac{\tau}{\tau_{an}}\right)^{\alpha}$, yielding:

$$G(\tau) = \frac{1}{V_{eff}\langle C\rangle}\left(1+\left(\frac{\tau}{\tau_{an}}\right)^{\alpha}\right)^{-1}\left(1+\frac{1}{K^2}\left(\frac{\tau}{\tau_{an}}\right)^{\alpha}\right)^{-\frac{1}{2}} \tag{22}$$

Equation (19) now becomes:

$$\tau_{an}^{\alpha} = \frac{r_0^2}{8\Gamma} \tag{23}$$

Using the anomalous diffusion model to fit our data, we found that in both types of gels, diffusion of all three QD samples and was hindered (α < 1) and the anomalous diffusion exponent was between 0.4 - 0.48 (Figure 26). Since there was no significant difference in the exponent for all samples, it is then valid to compare the magnitude of their effective diffusion coefficients, Γ.

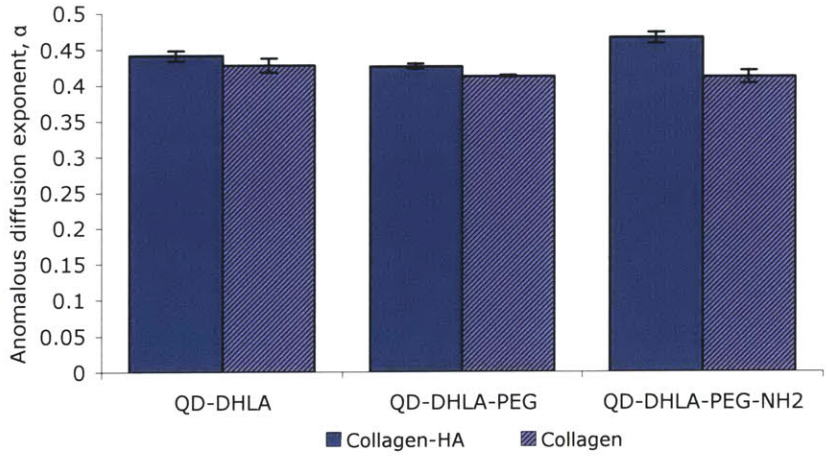

Figure 26. Anomalous diffusion exponent (α) values of QDs in gels. Values were extracted from experimental data fitted to an anomalous diffusion model. There was no significant difference across all samples. α was between 0.4 – 0.47, indicating anomalous subdiffusion. Error bars represent 1 S.E.M.

As can be seen in Figure 27, the transport coefficient of QD-DHLA-PEG was 70% higher than QD-DHLA (*) and 45% higher than QD-DHLA-PEG-NH_2 (✠) in collagen-HA composite gels. Similarly, QD-DHLA-PEG had the highest transport coefficient in the collagen gels and was 39% higher than QD-DHLA (❖) and 36% higher than QD-DHLA-PEG-NH_2 (☆). There was no significant difference between the transport coefficient of QDs with the same surface modification in the two gel types.

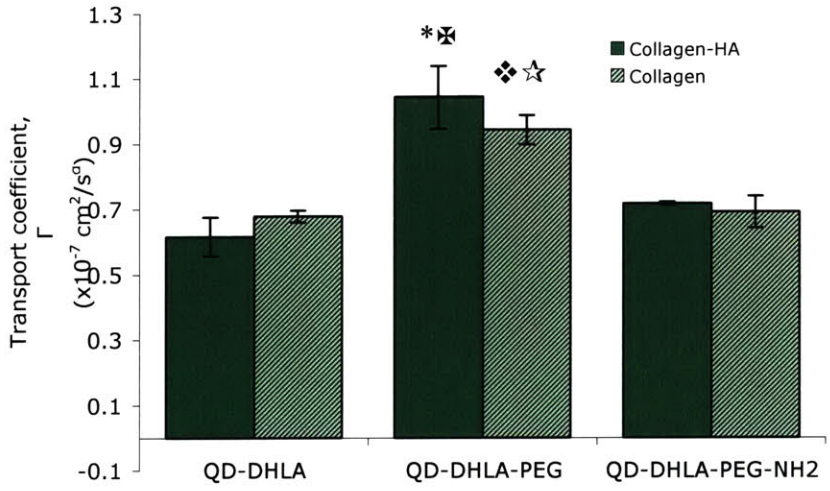

Figure 27. Transport coefficients of QDs in gels. Values were extracted from experimental data fitted to an anomalous diffusion model. * indicates statistical significance between QD-DHLA and QD-DHLA-PEG in collagen-HA ($p < 0.05$). ✠ indicates statistical significance between QD-DHLA-PEG-NH_2 and QD-DHLA-PEG in collagen-HA ($p < 0.05$). ❖ indicates statistical significance between QD-DHLA and QD-DHLA-PEG in collagen ($p < 0.05$). ☆ indicates statistical significance between QD-DHLA-PEG-NH_2 and QD-DHLA-PEG in collagen-HA ($p < 0.05$). Error bars represent 1 S.E.M.

Among the possible reasons for anomalous diffusion are environmental heterogeneities, obstruction, binding interactions, or physical contrains such as sieving, convection and percolation[84]. In this case, the diffusion of QDs might be

hindered by collagen fibers and also unassembled collagen in the void spaces of the gels[61]. The significant increase in the transport coefficient of the neutral QDs compared to both cationic and anionic QDs in both gels suggests that electrostatic interactions also play a role in hindering diffusion. Size alone cannot account for this difference. Collagen gels have a net positive charge and the introduction of HA in the composite gels introduces negative charges in the gel matrix. Thus, the binding and electrostatic repulsion effects could significantly reduce the transport of charged QDs, but the neutral QDs would be unaffected by such interactions.

An alternative model that describes the experimental data is a two-component free diffusion model, suggesting the coexistence of two populations with different mobilities. This model has been used to describe the transport of macromolecules in the tumor interstitium *in vivo*[57] and provides a good fit for our FCS curves (Figure 25). Equation can be extended to include a second species:

$$G(\tau) = G(0)\left[\Phi_1\left(1+\frac{\tau}{\tau_{D,1}}\right)^{-1}\left(1+\frac{\tau}{K^2\tau_{D,1}}\right)^{-\frac{1}{2}} + \Phi_2\left(1+\frac{\tau}{\tau_{D,2}}\right)^{-1}\left(1+\frac{\tau}{K^2\tau_{D,2}}\right)^{-\frac{1}{2}}\right] \quad (24)$$

Here, Φ_1 and Φ_2 represent the population fractions of each species while $\tau_{D,1}$ and $\tau_{D,2}$ are their respective diffusion times.

Measurements of the population fractions of QDs in collagen-HA composite gels (Figure 28) showed that a significantly higher percentage of QD-DHLA-PEG traveled in the fast phase compared to QD-DHLA (*). However, there was no statistically significant difference between QD-DHLA-PEG and QD-DHLA-PEG-NH_2.

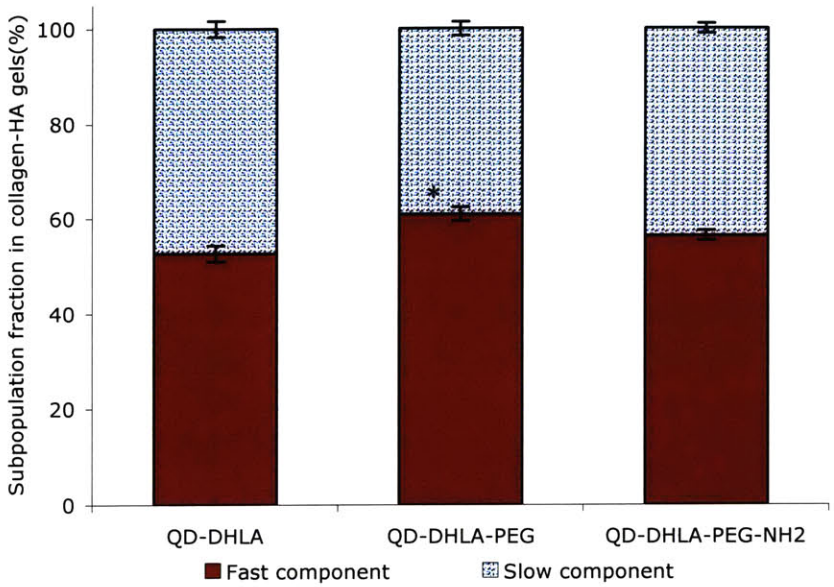

Figure 28. Subpopulation fraction of QDs in collagen-HA composite gels. *Experimental data show a significantly higher percentage of QD-DHLA-PEG in the fast component compared to QD-DHLA ($p < 0.05$). Error bars represent 1 S.E.M.

In the case of collagen gels (Figure 29), a significantly higher percentage of QD-DHLA-PEG traveled in the fast phase compared to QD-DHLA-PEG-NH_2 (*). There was no significant difference between QD-DHLA-PEG and QD-DHLA. Comparison between gel types with same QD samples also show not significant variation in their subpopulation fractions.

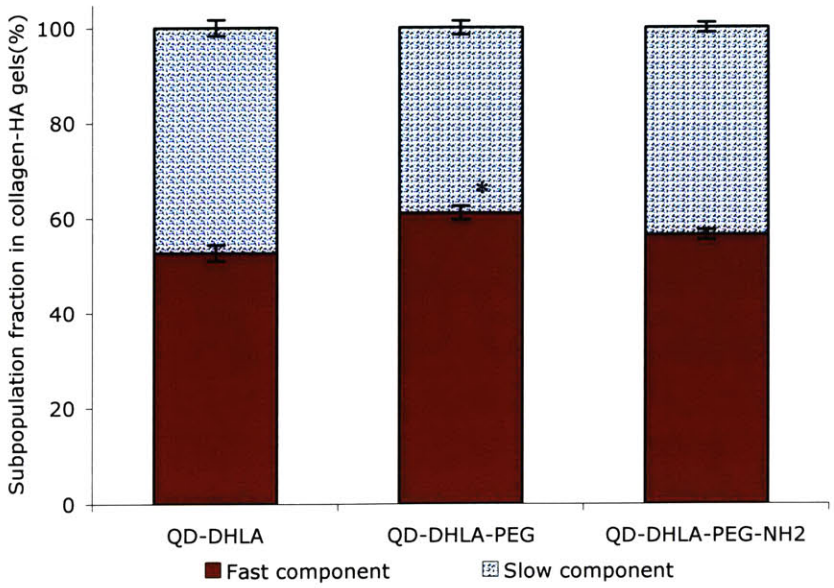

Figure 29. Subpopulation fraction of QDs in collagen gels. * Experimental data show a significantly higher percentage of QD-DHLA-PEG in the fast component compared to QD-DHLA ($p < 0.05$). Error bars represent 1 S.E.M.

Based on the measurements of the fast component diffusion coefficient (Figure 30), it appears that QD-DHLA-PEG moves the fastest in both gels, but the differences were not statistically significant, with the exception of the difference between QD-DHLA-PEG and QD-DHLA in the collagen gels (✠). The results of the slow component diffusion coefficient showed a significant difference between QD-DHLA and QD-DHLA-PEG-NH_2 in collagen-HA (✠), as well as a difference between QD-DHLA and QD-DHLA-PEG in collagen (✶). More interestingly, when comparing the two different gels, we observed that the diffusion coefficient for both cationic (✧) and anionic (❖) QDs were faster in the collagen-HA composite gel compared to the collagen gel.

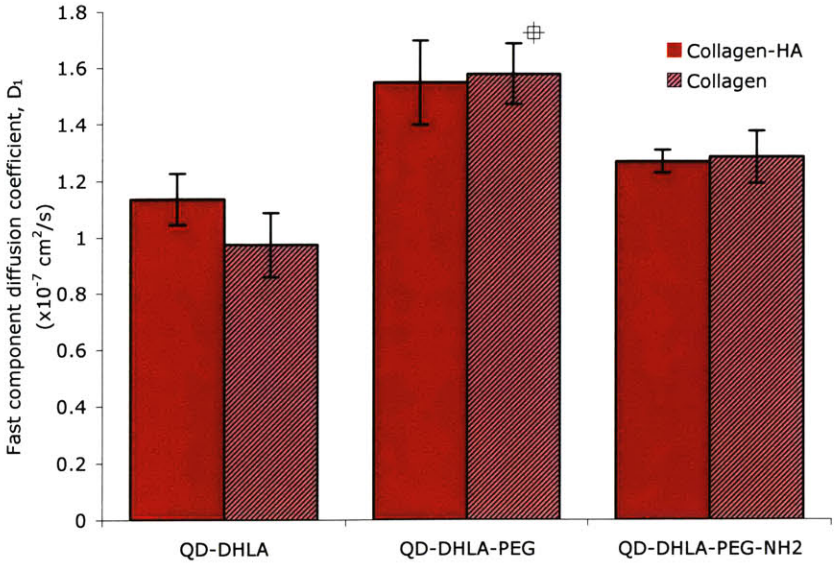

Figure 30. Fast component diffusion coefficients (D_1) of QDs in gels. ⌗ Experimental data show a significantly higher diffusion coefficient of QD-DHLA-PEG in the fast component compared to QD-DHLA ($p < 0.05$) in collagen. Error bars represent 1 S.E.M.

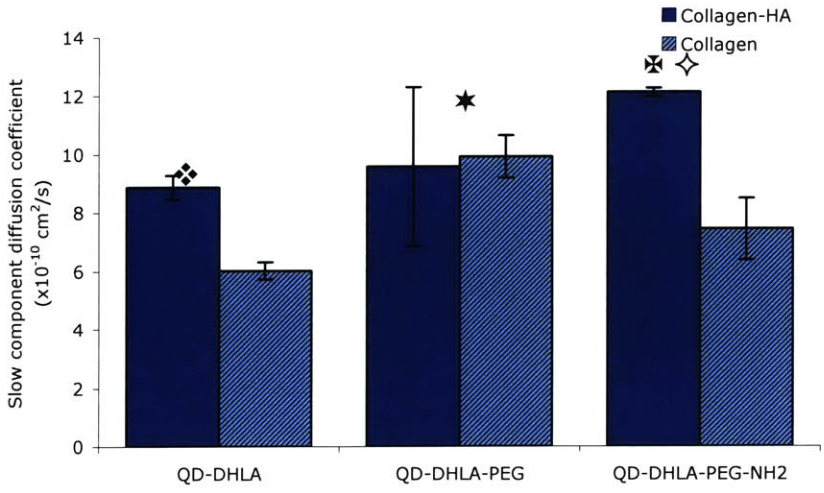

Figure 31. Slow component diffusion coefficients (D_2) of QDs in gels. ✶ Experimental data show a significantly higher diffusion coefficient of QD-DHLA-PEG than t compared to QD-DHLA in collagen. ✠ Diffusion coefficient of QD-DHLA-PEG-NH2 significantly higher than QD-DHLA in collagen-HA. ❖ Diffusion coefficient of QD-DHLA significantly higher in collagen-HA vs. collagen. ✧ Diffusion coefficient of QD-DHLA-PEG-NH_2 significantly higher in collagen-HA vs. collagen. For all cases listed, $p < 0.05$. Error bars represent 1 S.E.M.

This two-component model could depict a fast fluid-like phase and a slower, gel-like phase. Using this model, we would expect that the fast phase correspond to water-filled areas in the pores of the gels and the slow phase be correlated to the gel phase of collagen and HA. The effect of charge should be especially evident in the slow phase because of the interaction between the QDs with collagen and HA. Binding should result in a higher fraction of QDs traveling in the slow phase while electrostatic repulsion should increase the fraction of QDs traveling in the fast phase. Nonetheless, the results obtained through this fitting model did not support such a description and the effect of charge on the transport of could not be determined.

Despite the inconclusive results provided by this model, we can still gain some insight. For all samples and both gels, the slow component was slower than the fast component by approximately two orders of magnitude, which is agreement with the findings of in vivo studies[57]. In both gels, around 60% of QD-DHLA-PEG traveled in the fast phase, which matches in vivo subpopulation fraction measurements of a similar-size antibody - nonspecific IgG (hydrodynamic radius, 6.4 nm) in the tumor interstitium. The ratio of the fast component diffusion coefficient and the diffusion coefficient in free solution, D_1/D_0 of QD-DHLA-PEG is between 0.35 - 0.36, which also falls in the range reported previously. Of course, we must bear in mind that the *in vivo* measurements were

carried out in Mu89, which has higher collagen content compared to our gels. Thus, such comparisons are only useful in terms of the order of magnitude.

On the other hand, if we scale D_1 of QD-DHLA-PEG both gels from room temperature to 34°C (by the Stokes-Einstein equation), we obtain values around ranging from around 1.8×10^{-7} to 2.3×10^{-7} cm^2/s, which agrees with *in vivo* diffusion data for IgG in LS174T (1.29×10^{-7} - 2.77×10^{-7} cm^2/s) reported by Netti *et al.*[34] This comparison is much more informative, given that both of our gels have similar collagen and HA content as LS174T. It indicates that both the collagen and collagen-HA gels are good models of the tumor interstitium quantitatively. The fact that the fast component of our gel measurements resemble the overall diffusion coefficient measured by Netti *et al.* using fluorescence recovery after photobleaching (FRAP) also suggests that FRAP might not be able to detect the slow component which is two orders of magnitude smaller. The presence of such a slow moving component would probably be factored into the bound fraction that leads to incomplete recovery of the FRAP curve.

4.5 Conclusions

By utilizing MPFCS, the transport of charged QDs in gel models of the tumor interstitium was probed. Overall, the gels served as good models of the tumor for quantitative experiments. A simple diffusion model could not describe the diffusion of charged QDs in collagen and collagen-HA gels. Two other models - anomalous subdiffusion and two-component free diffusion were used to analyze the experimental data. Using the anomalous subdiffusion model, we conclude that charge played a significant role in the diffusion of QDs as neutral QD-DHLA-PEG diffused the fastest compared to the cationic QD-DHLA-PEG-NH_2 and anionic QD-DHLA. The results using a two-component diffusion model did not provide a clear effect of charge on QD diffusion.

Although the results were statistically significant, the lack of a big difference between different charged QDs could be due to their relatively small size, since Johnson *et al.* reported that the ionic strength of agarose gels had no effect on the diffusion of BSA[60]. Perhaps a bigger difference in the zeta potential of each sample is also needed and/or a higher concentration of HA in order for electrostatic interactions to play a more significant role. Alternatively, our measurements might not have provided a complete picture because FCS measurements were limited to areas free from aggregation and high concentration. Thus, there is a need to combine FCS with other techniques, such

as FRAP to provide flexibility in measurements and construct a more detailed picture of the effect of surface charge on nanoparticle transport in the tumor interstitium.

References

1. Jemal, A. et al. Cancer statistics, 2007. *CA Cancer J Clin* **57**, 43-66 (2007).
2. Ferrari, M. Cancer nanotechnology: opportunities and challenges. *Nat Rev Cancer* **5**, 161-71 (2005).
3. Kim, G.J. & Nie, S. Targeted cancer nanotherapy. *Materials Today* **8**, 28-33 (2005).
4. Desai, N. Poster discussion session from the San Antonio Breast Cancer Society. *San Antonio Breast Cancer Society, San Antonio, Tx* (2004).
5. Jain, R.K. The next frontier of molecular medicine: delivery of therapeutics. *Nature Medicine* **4**, 655-657 (1998).
6. Jain, R.K. Delivery of molecular and cellular medicine to solid tumors. *Adv. Drug Deliv. Rev.* **46**, 149-168 (2001).
7. Ehdaie, B. Application of Nanotechnology in Cancer Research: Review of Progress in the National Cancer Institute's Alliance for Nanotechnology. *Int J Biol Sci* **3**, 108-10 (2007).
8. Whitesides, G.M. The 'right' size in nanobiotechnology. *Nat Biotechnol* **21**, 1161-5 (2003).
9. La Van, D.A., McGuire, T. & Langer, R. Small-scale systems for in vivo drug delivery. *Nature Biotechnol.* **21**, 1184-1191 (2003).
10. McNeil, S.E. Nanotechnology for the biologist. *J Leukoc Biol* **78**, 585-94 (2005).
11. Chen, L.T. & Weiss, L. The role of the sinus wall in the passage of erythrocytes through the spleen. *Blood* **41**, 529-37 (1973).
12. Bailey, F.R., Copenhaver, W.M., Bunge, R.P. & Bunge, M.B. *Bailey's Textbook of Histology*, (Williams & Wilkins, Baltimore, MD, 1971).
13. Braet, F. et al. Structure and dynamics of the fenestrae-associated cytoskeleton of rat liver sinusoidal endothelial cells. *Hepatology* **21**, 180-9 (1995).
14. Morawski, A.M. et al. Targeted nanoparticles for quantitative imaging of sparse molecular epitopes with MRI. *Magn Reson Med* **51**, 480-6 (2004).
15. Storm, G., Belliot, S.O., Daemen, T. & Lasic, D.D. Surface modification of nanoparticles to oppose uptake by the mononuclear phagocyte system. *Advanced Drug Delivery Reviews* **17**, 31-48 (1995).
16. Jain, R.K. Transport of molecules, particles, and cells in solid tumors. *Annu Rev Biomed Eng* **1**, 241-63 (1999).
17. Matsumura, Y. & Maeda, H. A new concept for macromolecular therapies in cancer chemotherapy: mechanisms of tumortropic accumulation of proteins and the antitumor agents SMANCS. *Cancer Res.* **6**, 6397-6392 (1986).
18. Hobbs, S.K. et al. Regulation of transport pathways in tumor vessels: role of tumor type and microenvironment. *Proc Natl Acad Sci U S A* **95**, 4607-12 (1998).
19. Yuan, F. et al. Vascular permeability in a human tumor xenograft: molecular size dependence and cutoff size. *Cancer Research* **55**, 3752-3756 (1995).
20. Duncan, R. The dawning era of polymer therapeutics. *Nature Rev. Drug Discov.* **2**, 347-360 (2003).
21. Gref, R. et al. Biodegradable long-circulating polymeric nanospheres. *Science* **263**, 1600-3 (1994).
22. Moghimi, S.M. & Szebeni, J. Stealth liposomes and long circulating nanoparticles: critical issues in pharmacokinetics, opsonization and protein-binding properties. *Prog Lipid Res* **42**, 463-78 (2003).
23. Campbell, R.B. et al. Cationic charge determines the distribution of liposomes between the vascular and extravascular compartments of tumors. *Cancer Research* **62**, 6831-6836 (2002).
24. Krasnici, S. et al. Effect of the surface charge of liposomes on their uptake by angiogenic tumor vessels. *Int J Cancer* **105**, 561-567 (2003).
25. Thurston, G. et al. Cationic liposomes target angiogenic endothelial cells in tumors and chronic inflammation in mice. *J Clin Invest* **101**, 1401-1413 (1998).
26. Murray, C.B., Norris, D.J. & Bawendi, M.G. Synthesis and characterization of nearly monodisperse CdE (E=S, Se, Te) semiconductor nanocrystallites

. *J. Am. Chem. Soc.* **115**, 8706-8715 (1993).

27. Larson, D.R. et al. Water-soluble quantum dots for multiphoton fluorescence imaging in vivo. *Science* **300**, 1434-1436 (2003).
28. Stroh, M. et al. Quantum dots spectrally distinguish multiple species within the tumor milieu in vivo. *Nat Med* **11**, 678-682 (2005).
29. Tada, H., Higuchi, H., Wanatabe, T.M. & Ohuchi, N. In vivo real-time tracking of single quantum dots conjugated with monoclonal anti-HER2 antibody in tumors of mice. *Cancer Res* **67**, 1138-44 (2007).
30. Kim, S. et al. Near-infrared fluorescent type II quantum dots for sentinel lymph node mapping. *Nat Biotechnol* **22**, 93-7 (2004).
31. Soltesz, E.G. et al. Sentinel lymph node mapping of the gastrointestinal tract by using invisible light. *Ann Surg Oncol* **13**, 386-96 (2006).
32. Gao, X., Cui, Y., Levenson, R.M., Chung, L.W. & Nie, S. In vivo cancer targeting and imaging with semiconductor quantum dots. *Nat Biotechnol* **22**, 969-76 (2004).
33. Aukland, K. & Reed, R. Interstitial-lymphatic mechanisms in the control of extracellular fluid volume. *Physiol Rev* **73**, 1-78 (1993).
34. Netti, P., Berk, D., Swartz, M., Grodzinsky, A. & Jain, R. Role of extracellular matrix assembly in interstitial transport in solid tumors. *Cancer Res* **60**, 2497-503 (2000).
35. Jain, R.K. Transport of molecules in the tumor interstitium: a review. *Cancer Research* **47**, 3039-3051 (1987).
36. Gersh, I. & Catchpole, H.R. The nature of ground substance of connective tissue. *Perspect Biol Med* **3**, 282-319 (1960).
37. Laurent, T.C. Structure, function, and turnover of the extracellular matrix. *Adv. Microcirc.* **13**, 15-34 (1987).
38. Gullino, P.M. & Grantham, F.H. The influence of the host and the neoplastic cell population on the collagen content of a tumor mass. *Cancer Res* **23**, 648-653 (1963).
39. Scott, J.E. Collagen--proteoglycan interactions. Localization of proteoglycans in tendon by electron microscopy. *Biochem J* **187**, 887-91 (1980).
40. Pluen, A. et al. Role of tumor-host interactions in interstitial diffusion of macromolecules: cranial vs. subcutaneous tumors. *Proc Natl Acad Sci USA* **98**, 4628-33 (2001).
41. Oxlund, H., Manschot, J. & Viidik, A. The role of elastin in the mechanical properties of skin. *J Biomech* **21**, 213-8 (1988).
42. Prehm, P. Hyaluronate is synthesized at plasma membranes. *Biochem J* **220**, 597-600 (1984).
43. Roden, L. Structure and metabolism of connective tissue proteoglycans. in *The Biochemistry of Glycoproteins and Proteoglycans* (ed. Lennarz, W.L.) 267-371 (Plenum, New York, 1980).
44. Leach, J.B. & Schimdt, C.E. Hyaluronan. in *Encyclopedia of Biomaterials amd Biomedical Engineering* 779-789 (Markus Dekker, Inc., New York, 2004).
45. Laurent, T.C. & Fraser, J.R. Hyaluronan. *Faseb J* **6**, 2397-404 (1992).
46. Comper, W.D. & Laurent, T.C. Physiological function of connective tissue polysaccharides. *Physiol Rev* **58**, 255-315 (1978).
47. Li, S. & Katz, E. An electrostatic model for collagen fibrils. The interaction of reconstituted collagen with Ca++, Na+, and Cl-. *Biopolymers* **15**, 1439-60 (1976).
48. Wiig, H., Gyenge, C.C. & Tenstad, O. The interstitial distribution of macromolecules in rat tumours is influenced by the negatively charged matrix components. *J Physiol* **567**, 557-67 (2005).
49. Bert, J.L. & Pearce, R.H. The interstitium and microvascular exchange. in *Handbook of Physiology*, Vol. IV (eds. Renkin, E.M. & Michel, C.C.) 521-547 (American Physiology Society, Bethasda, MD, 1984).
50. Katz, E.P. & Li, S.T. The intermolecular space of reconstituted collagen fibrils. *J Mol Biol* **73**, 351-69 (1973).
51. Granger, H.J., Dhar, J. & Chen, H.I. Dynamics and control of transmicrovascular fluid exchange. in *Edema* (ed. Staub, N.C.) 189-228 (Raven, New York, 1984).
52. Boucher, Y., Baxter, L.T. & Jain, R.K. Interstitial pressure gradients in tissue-isolated and subcutaneous tumors: implications for therapy. *Cancer Res* **50**, 4478-84 (1990).

53. Netti, P.A. et al. Enhancement of fluid filtration across tumor vessels: implication for delivery of macromolecules. *Proc Natl Acad Sci U S A* **96**, 3137-42 (1999).
54. Nugent, L. & Jain, R. Extravascular diffusion in normal and neoplastic tissues. *Cancer Res* **44**, 238-44 (1984).
55. Gullino, P.M., Grantham, F.H. & Smith, S.H. The Interstitial Water Space of Tumors. *Cancer Res* **25**, 727-31 (1965).
56. Nugent, L. & Jain, R. Plasma pharmacokinetics and interstitial diffusion of macromolecules in a capillary bed. *Am J Physiol* **246**, H129-37 (1984).
57. Alexandrakis, G. et al. Two-photon fluorescence correlation microscopy reveals the two-phase nature of transport in tumors. *Nature Medicine* **10**, 203-207 (2004).
58. Pluen, A., Netti, P.A., Jain, R.K. & Berk, D.A. Diffusion of macromolecules in agarose gels: comparison of linear and globular configurations. *Biophys J* **77**, 542-52 (1999).
59. Deen, W.M., Bohrer, M.P. & Epstein, N.B. Effects of molecular size and configuration on diffusion in microporous membranes. *Am. Inst. Chem. Eng. J.* **27**, 952-959 (1981).
60. Johnson, E., Berk, D., Jain, R. & Deen, W. Diffusion and partitioning of proteins in charged agarose gels. *Biophys J* **68**, 1561-8 (1995).
61. Ramanujan, S. et al. Diffusion and convection in collagen gels: implications for transport in the tumor interstitium. *Biophys J* **83**, 1650-60 (2002).
62. Magde, M., Elson, E. & Webb, W. Fluorescence correlation spectroscopy. II. An experimental realization. *Biopolymers* **13**, 29-61 (1974).
63. Elson, E. Fluorescence correlation spectroscopy. I. Conceptual basis and theory. *Biopolymers* **13**, 1-27 (1974).
64. Magde, D., Webb, W.W. & Elson, E.L. Fluorescence correlation spectroscopy. III. Uniform translation and laminar flow. *Biopolymers* **17**, 361 - 376 (1978).
65. Icenogle, R.D. & Elson, E.L. Fluorescence correlation spectroscopy and photobleaching recovery of multiple binding reactions. II. FPR and FCS measurements at low and high DNA concentrations. *Biopolymers* **22**, 1949-66 (1983).
66. Icenogle, R.D. & Elson, E.L. Fluorescence correlation spectroscopy and photobleaching recovery of multiple binding reactions. I. Theory and FCS measurements. *Biopolymers* **22**, 1919-48 (1983).
67. Elson, E.L. & Webb, W.W. Concentration correlation spectroscopy: a new biophysical probe based on occupation number fluctuations. *Annu Rev Biophys Bioeng* **4**, 311-34 (1975).
68. Elson, E. Quick tour of fluorescence correlation spectroscopy from its inception. *J Biomed Opt* **9**, 857-64 (2004).
69. Berland, K.M., So, P.T. & Gratton, E. Two-photon fluorescence correlation spectroscopy: method and application to the intracellular environment. *Biophys J* **68**, 694-701 (1995).
70. Qian, H. & Elson, E.L. Analysis of confocal laser-microscope optics for 3-D fluorescence correlation spectroscopy. *Appl. Optics* **30**, 1185-1195 (1991).
71. Rigler, R., Mets, U., Widengren, J. & Kask, P. Fluorescence correlation spectroscopy with high count rate and low background: analysis of translational diffusion. *Eur. Biophys. J,* **22**, 169-175 (1993).
72. Schwille, P., Haupts, U., Maiti, S. & Webb, W.W. Molecular dynamics in living cells observed by fluorescence correlation spectroscopy with one- and two-photon excitation. *Biophys J* **77**, 2251-65 (1999).
73. Liedl, T., Keller, S., Simmel, F., Rädler, J. & Parak, W. Fluorescent nanocrystals as colloidal probes in complex fluids measured by fluorescence correlation spectroscopy. *Small (Weinheim an der Bergstrasse, Germany)* **1**, 997-1003 (2005).
74. Schwille, P. & Haustein, E. Fluorescence correlation spectroscopy: An introduction to its concepts and applications. (Biophys. J.).
75. Zipfel, W.R., Williams, R.M. & Webb, W.W. Nonlinear magic: multiphoton microscopy in the biosciences. *Nat Biotechnol* **21**, 1369-77 (2003).
76. Periasamy, A., Zipfel, W.R. & Webb, W.W. (eds.). *Methods in cellular imaging*, 434 (Oxford University Press, Oxford, 2001).
77. Richards, B. & Wolf, E. Electromagnetic diffraction in the optical systems II. Structure of the image field in a planatic system. *Proc. R. Soc. Lond. Ser. A* **253**, 358-379 (1959).

78. Denk, W., Strickler, J.H. & Webb, W.W. Two-photon laser scanning fluorescence microscopy. *Science* **248**, 73-6 (1990).
79. Iyer, V., Rossow, M., Waxham, M. & Periasamy, A. Focal volume characterization using multiphoton fluorescence correlation spectroscopy (MP-FCS). *Proceedings of SPIE* (2004).
80. Neil, M.A.A., Juskaitis, R. & Wilson, T. Method of obtaining optical sectioning by using structured light in a conventional microscope *Optics Letters* **22**, 1905-1907 (1997).
81. Jain, R.K., Stock, R.J., Chary, S.R. & Rueter, M. Convection and diffusion measurements using fluorescence recovery after photobleaching and video image analysis: in vitro calibration and assessment. *Microvasc Res* **39**, 77-93 (1990).
82. Doose, S., Tsay, J., Pinaud, F. & Weiss, S. Comparison of photophysical and colloidal properties of biocompatible semiconductor nanocrystals using fluorescence correlation spectroscopy. *Anal Chem* **77**, 2235-42 (2005).
83. Nirmal, M. et al. Fluorescence intermittency in single cadmium selenide nanocrystals. *Nature* **383**, 802-804 (1996).
84. Periasamy, N. & Verkman, A.S. Analysis of fluorophore diffusion by continuous distributions of diffusion coefficients: application to photobleaching measurements of multicomponent and anomalous diffusion. *Biophys J.* **75**, 557-567 (1998).